PHYSICS OF FLUIDS **25**, 044105 (2013)

Onset of buoyancy-driven convection in Cartesian and cylindrical geometries

Philip C. Myint[1,2,a)] and Abbas Firoozabadi[1,3,b)]
[1]*Department of Chemical and Environmental Engineering, Yale University, 9 Hillhouse Avenue, New Haven, Connecticut 06511, USA*
[2]*Atmospheric, Earth, and Energy Division, Lawrence Livermore National Laboratory, Livermore, California 94550, USA*
[3]*Reservoir Engineering Research Institute, Palo Alto, California 94301, USA*

(Received 13 September 2012; accepted 25 March 2013; published online 25 April 2013)

We perform a linear stability analysis to examine the onset of buoyancy-driven convection relevant to subsurface carbon dioxide sequestration in confined, porous Cartesian and cylindrical domains. Our work amends the analysis in an earlier study on cylindrical geometries. We consider Cartesian geometries where the aspect ratio between the two horizontal dimensions is not necessarily equal to one. Two key elements of the stability analysis are: (1) the critical time and (2) the critical wavenumber. Lateral boundaries have a much greater influence on the critical wavenumber than on the critical time. The confinement due to these boundaries impedes the onset of convection to the extent that convection cannot even occur in domains that are smaller than a certain size. Large aspect ratios can significantly reduce boundary effects. Patterns of the earliest-growing perturbation mode in the horizontal plane reveal many interesting dynamics which have not been examined in previous stability analyses. We illustrate several differences between patterns in Cartesian geometries and patterns in cylindrical geometries. Based on observations from earlier papers, we hypothesize that the contrasts between the Cartesian and cylindrical patterns may lead to significantly different behavior in the two geometries after the onset of convection. Our results may guide future numerical studies that can investigate this hypothesis and may help with understanding the onset of buoyancy-driven convection in real systems where lateral boundary effects are significant. © *2013 AIP Publishing LLC*. [http://dx.doi.org/10.1063/1.4801930]

I. INTRODUCTION

Buoyancy-driven flows have generated much interest since the pioneering work of Lord Rayleigh and Henri Bénard over a century ago.[1–12] A classic example involving such flows is the Horton-Rogers-Lapwood problem, which considers a vertical thermal gradient imposed between two boundaries that enclose a fluid-filled porous medium.[13,14] Before the onset of convection, the temperature profile is steady and increases linearly in the downward direction. This creates a buoyantly unstable situation where heavier, colder fluid lies on top of lighter, hotter fluid. One may perform a linear stability analysis to show that above a critical Rayleigh number (i.e., for a sufficiently strong thermal gradient), the buoyancy-driven instabilities may lead to the onset of convection within the porous medium. Many aspects of the Horton-Rogers-Lapwood problem have been studied.[15,16] For example, several authors have performed linear stability analyses to investigate the effect of lateral boundaries in Cartesian and cylindrical geometries on the onset of convection.[17–22] A related, yet different problem examines a fluid-filled porous medium where the temperature is initially uniform everywhere except at the top boundary, which is suddenly cooled to a lower temperature and held

a)Electronic mail: philip.myint@yale.edu
b)Electronic mail: abbas.firoozabadi@yale.edu

fixed at that temperature. (Equivalently, we could instead have a bottom boundary that is suddenly heated and held fixed at the higher temperature.) Like in the Horton-Rogers-Lapwood problem, the state of the fluid before the onset of convection, which is called the base state, is buoyantly unstable. The difference is that the base state in the second problem is described by a transient (unsteady) temperature profile that obeys the one-dimensional heat equation. The linear stability analysis for this problem calculates two key quantities: (1) the critical time and (2) the critical wavenumber. Onset of convection occurs at the critical time. It represents the first instance when the base state becomes unstable. The stability analysis works by subjecting the base state to small wave-like perturbations; the critical wavenumber characterizes the earliest-growing (most unstable) perturbation mode.

Linear stability analyses are also important for modeling the dissolution of carbon dioxide (CO_2) in saline aquifers for geological sequestration.[23–25] Carbon dioxide is one of the few common atmospheric gases that increase the density of water upon dissolution.[26] The density increase may lead to the onset of buoyancy-driven convection in the aqueous phase. Convection is desirable for sequestration in saline aquifers because it can greatly enhance the CO_2 dissolution rate into the aqueous phase. Thus, it is of interest to determine when the onset of convection occurs. For CO_2 sequestration, we may consider CO_2 transport through a water-saturated porous medium that is initially devoid of CO_2 everywhere except at the top boundary, which is held fixed at a constant CO_2 concentration. This setup follows the same governing equations and initial/boundary conditions as its thermal analogue described in the preceding paragraph. As a result, they are mathematically equivalent and may be treated interchangeably. We refer to both of them collectively as the transient base state problem. Many authors have performed stability analyses[27–37] to determine the critical time and the critical wavenumber for the transient base state problem. These studies are based on methods introduced in earlier papers on porous media[38,39] and open-space (cavities without porous media).[40–45] One issue that arises is that there is no universally accepted mathematical definition of the critical time. Systematic comparisons[35–37,46] among the various studies in the literature[27–37] have found that reported critical times may differ by a factor of several-fold. How to best define the critical time is still an open question. Nevertheless, this is not of concern for the present work because we will use only one definition, the one introduced by Slim and Ramakrishnan,[35] which yields the earliest onset of convection (the smallest critical time) reported in the literature.

In this article, we present a linear stability analysis of the transient base state problem, and more specifically the CO_2 sequestration problem, to determine conditions for the onset of buoyancy-driven convection in confined, porous Cartesian, and cylindrical domains. Most stability analyses of the transient base state problem[27–33,35–37] have neglected lateral boundaries and focus on unconfined domains. Kim *et al.*[34] have studied CO_2 dissolution in cylindrical geometries. They use boundary conditions in which the radial CO_2 diffusive flux and the radial derivative of the vertical velocity must vanish at the center of the cylinder. Their stability analysis is based on "propagation theory," in which the perturbations do not depend explicitly on time.[32,46] Instead, time enters the equations implicitly as a parameter. We use more physically realistic boundary conditions and allow the perturbations to depend explicitly on time. In this sense, the present study amends the analysis of Kim *et al.*[34] Our work also considers confined Cartesian geometries where the aspect ratio between the two horizontal dimensions is not necessarily equal to one. We present our formulation in Sec. II. We analyze the influence of the lateral boundaries on the critical time and the critical wavenumber in Sec. III. We show that the confinement effect may be appreciable in laboratory-scale experiments[47–49] and in numerical simulations. The patterns of the earliest-growing mode in the horizontal plane reveal many interesting features of the dynamics. Section IV illustrates several ways in which patterns in Cartesian geometries are distinct from patterns in cylindrical geometries. We compare our patterns with those from a numerical study[50] of the transient base state problem and from stability analyses of the Horton-Rogers-Lapwood problem in Cartesian[17,18] and cylindrical[19] geometries. Based on observations from earlier papers, we hypothesize that the contrasts between the Cartesian and cylindrical patterns may lead to significantly different behavior in the two geometries after the onset of convection. Our results may guide future numerical studies that can investigate this hypothesis. We conclude with a summary of our main findings.

II. FORMULATION

A. Governing equations and initial/boundary conditions

Our system is an isothermal binary mixture of CO_2 and water in a porous medium of height H that is homogeneous in its porosity ϕ and permeability k. In both Cartesian and cylindrical coordinates, the z axis is centered at the top boundary and points upward. The viscosity μ and diffusion coefficient D are constants. The diffusive flux is given by Fick's law as $\mathbf{J} = -\phi\rho D\nabla\omega$, where ρ is the mass density and ω is the CO_2 mass fraction. The medium is initially composed of water only, except at the top boundary, which is saturated with CO_2 at a fixed mass fraction ω_{sat}. Fluid flow is governed by Darcy's law, which relates the velocity field $\mathbf{q}$ to the pressure gradient ∇p and gravitational force $-\rho g\nabla z$. We also have the continuity equation and a CO_2 species balance equation, which we use with the Boussinesq approximation. The governing equations may be expressed as

$$\mathbf{q} = -\frac{k}{\mu}\left(\nabla p + \rho g\nabla z\right), \tag{1}$$

$$\nabla\cdot\mathbf{q} = 0, \tag{2}$$

$$\frac{\partial\omega}{\partial t} = -\frac{\mathbf{q}}{\phi}\cdot\nabla\omega + D\nabla^2\omega. \tag{3}$$

The density obeys the linear constitutive equation

$$\rho = \rho_0(1+\alpha\omega), \tag{4}$$

where ρ_0 and α are constants. The maximum increase in density from dissolution is $\Delta\rho = \rho_0\alpha\omega_{\text{sat}}$. Using (4) and letting $P = p + \rho_0 gz$, we may express (1) as

$$\mathbf{q} = -\frac{k}{\mu}\left(\nabla P + \rho_0\alpha\omega g\nabla z\right). \tag{5}$$

We follow earlier works[30,35,51] and nondimensionalize equations (2), (3), and (5) with a velocity scale $\mho = k\Delta\rho g/\mu$, a length scale $\ell = (\phi D)/\mho = (D\phi\mu)/(k\Delta\rho g)$, and a time scale $\tau = (\phi\ell)/\mho = D\left[(\phi\mu)/(k\Delta\rho g)\right]^2$. Using these quantities, we introduce the variables $\tilde{t} = t/\tau$, $\tilde{\omega} = \omega/\omega_{\text{sat}}$, $\tilde{P} = P/(\Delta\rho g\ell)$. In Cartesian geometries, the position is specified by $\mathbf{r} = (x, y, z)^T$. Vectorial quantities are represented by column vectors following the usual mathematical convention. We nondimensionalize $\mathbf{r}$ and $\mathbf{q}$ according to $\tilde{\mathbf{r}} = (\tilde{x}, \tilde{y}, \tilde{z})^T = (x, y, z)^T/\ell$ and $\tilde{\mathbf{q}} = \left(\tilde{q}_x, \tilde{q}_y, \tilde{q}_z\right)^T = \left(q_x, q_y, q_z\right)^T/\mho$. The size of the domain in the $\tilde{x}$ direction is the width $\tilde{W} = W/\ell$ so that $\tilde{x}$ ranges from 0 to $\tilde{W}$. The size in $\tilde{y}$ is $A\tilde{W}$, where A is the aspect ratio. In cylindrical geometries, we have $\tilde{\mathbf{r}} = (\tilde{r}, \theta, \tilde{z})^T = (r/\ell, \theta, z/\ell)^T$, and $\tilde{\mathbf{q}} = (\tilde{q}_r, \tilde{q}_\theta, \tilde{q}_z)^T = (q_r, q_\theta, q_z)^T/\mho$. The radius is R and $\tilde{r}$ ranges from 0 to $\tilde{R} = R/\ell$. We do not normalize θ by 2π since doing so does not simplify the equations. The governing equations (2), (3), and (5) in nondimensionalized form are

$$\tilde{\mathbf{q}} = -\nabla\tilde{P} - \tilde{\omega}\nabla\tilde{z}, \tag{6}$$

$$\nabla\cdot\tilde{\mathbf{q}} = 0, \tag{7}$$

$$\frac{\partial\tilde{\omega}}{\partial\tilde{t}} = -\tilde{\mathbf{q}}\cdot\nabla\tilde{\omega} + \nabla^2\tilde{\omega}. \tag{8}$$

In this choice of scaling, the Rayleigh number $\text{Ra} = (k\Delta\rho gH)/(\phi\mu D)$ does not appear in the governing equations. Instead, Ra appears in the location of the boundary so that the porous domain is defined in the range $-\text{Ra} \le \tilde{z} \le 0$. At the onset of convection, the CO_2 concentration will be small at the bottom boundary for sufficiently tall porous domains. Slim and Ramakrishnan[35] have shown that the results of the stability analysis are independent of the Rayleigh number for domains where

$\mathrm{Ra} > 75$. Following Bestehorn,[52] a velocity field $\tilde{\mathbf{q}}$ that satisfies (7) can be represented by two scalar functions Φ and Ψ as

$$\tilde{\mathbf{q}} = \nabla \times (\Phi \nabla \tilde{z}) + \nabla \times [\nabla \times (\Psi \nabla \tilde{z})]. \tag{9}$$

We now show that $\nabla \times (\Phi \nabla \tilde{z}) = \mathbf{0}$ for this problem. Taking the curl of (6) and using (9), we obtain $\nabla_{\mathrm{h}}^2 \Phi = 0$, where ∇_{h}^2 is the horizontal Laplacian. This operator is defined as $\nabla_{\mathrm{h}}^2 = \partial^2/\partial \tilde{x}^2 + \partial^2/\partial \tilde{y}^2$ and $\nabla_{\mathrm{h}}^2 = \partial^2/\partial \tilde{r}^2 + (1/\tilde{r})\partial/\partial \tilde{r} + (1/\tilde{r}^2)\partial^2/\partial \theta^2$ in Cartesian and cylindrical coordinates, respectively. Let $\mathcal{D}$ be an arbitrary region in the horizontal plane ($\tilde{x}\tilde{y}$ or $\tilde{r}\theta$ plane) enclosed by a positively oriented, simple closed curve $\mathcal{C}$. Green's theorem states that

$$\int_{\mathcal{D}} \nabla_{\mathrm{h}}^2 \Phi \, \mathrm{d}\mathcal{A} = -\oint_{\mathcal{C}} [\nabla \times (\Phi \nabla \tilde{z})] \cdot \mathrm{d}\tilde{\mathbf{r}}, \tag{10}$$

where $\mathrm{d}\mathcal{A}$ denotes $\mathrm{d}\tilde{x}\,\mathrm{d}\tilde{y}$ or $\tilde{r}\,\mathrm{d}\tilde{r}\,\mathrm{d}\theta$. Since the integrand in the left-hand side of (10) is zero and the region $\mathcal{D}$ is arbitrary, $\nabla \times (\Phi \nabla \tilde{z})$ must identically be zero. Thus, we may compute the velocity components from a single scalar function Ψ so that (9) becomes

$$\tilde{\mathbf{q}} = \nabla \times [\nabla \times (\Psi \nabla \tilde{z})]. \tag{11}$$

In Cartesian coordinates, the components of $\tilde{\mathbf{q}}$ are $\tilde{q}_x = \partial^2 \Psi/\partial \tilde{x}\partial \tilde{z}$, $\tilde{q}_y = \partial^2 \Psi/\partial \tilde{y}\partial \tilde{z}$, and $\tilde{q}_z = -\nabla_{\mathrm{h}}^2 \Psi$. In cylindrical coordinates, they are $\tilde{q}_r = \partial^2 \Psi/\partial \tilde{r}\partial \tilde{z}$, $\tilde{q}_\theta = (1/\tilde{r})\partial^2 \Psi/\partial \theta \partial \tilde{z}$, and $\tilde{q}_z = -\nabla_{\mathrm{h}}^2 \Psi$. Taking twice the curl of (6) and using (7) and (11), we have

$$\nabla^2 \Psi = \tilde{\omega}. \tag{12}$$

The base state is characterized by a concentration profile $\tilde{\omega}_{\mathrm{base}}(\tilde{z}, \tilde{t})$ that satisfies

$$\frac{\partial \tilde{\omega}_{\mathrm{base}}}{\partial \tilde{t}} = \frac{\partial^2 \tilde{\omega}_{\mathrm{base}}}{\partial \tilde{z}^2}, \tag{13}$$

$$\tilde{\omega}_{\mathrm{base}}(\tilde{z}, 0) = 0, \quad -\mathrm{Ra} \le \tilde{z} < 0, \tag{14}$$

$$\left.\frac{\partial \tilde{\omega}_{\mathrm{base}}}{\partial \tilde{z}}\right|_{(\tilde{z}=-\mathrm{Ra}, \tilde{t})} = 0, \quad \forall \tilde{t}, \tag{15}$$

$$\tilde{\omega}_{\mathrm{base}}(\tilde{z} = 0, \tilde{t}) = 1, \quad \forall \tilde{t}. \tag{16}$$

The solution to (13) with the initial/boundary conditions (14)–(16) is[35]

$$\tilde{\omega}_{\mathrm{base}}(\tilde{z}, \tilde{t}) = 1 + \frac{4}{\pi} \sum_{l=1}^{\infty} \frac{1}{2l-1} \sin\left[\left(l - \frac{1}{2}\right)\frac{\pi \tilde{z}}{\mathrm{Ra}}\right] \exp\left\{-\left[\left(l - \frac{1}{2}\right)\frac{\pi}{\mathrm{Ra}}\right]^2 \tilde{t}\right\}. \tag{17}$$

Bulk fluid motion is absent in the base state ($\tilde{\mathbf{q}}_{\mathrm{base}} = \mathbf{0}$), which requires that the scalar function Ψ_{base} be a function of only $\tilde{z}$ and $\tilde{t}$. From (12), we see that $\Psi_{\mathrm{base}}(\tilde{z}, \tilde{t})$ satisfies

$$\nabla^2 \Psi_{\mathrm{base}} = \frac{\partial^2 \Psi_{\mathrm{base}}}{\partial \tilde{z}^2} = \tilde{\omega}_{\mathrm{base}}. \tag{18}$$

We may express perturbations to the base state as $\Psi' = \Psi - \Psi_{\mathrm{base}}$ and $\tilde{\omega}' = \tilde{\omega} - \tilde{\omega}_{\mathrm{base}}$. We substitute the perturbations into (8) and (12), use (13) and (18), and linearize to obtain

$$\frac{\partial \tilde{\omega}'}{\partial \tilde{t}} = \nabla_{\mathrm{h}}^2 \Psi' \frac{\partial \tilde{\omega}_{\mathrm{base}}}{\partial \tilde{z}} + \nabla^2 \tilde{\omega}', \tag{19}$$

$$\nabla^2 \Psi' = \tilde{\omega}'. \tag{20}$$

We use Ψ' rather than work directly with the velocity field like in previous stability analyses of the transient base state problem[27–37] because using Ψ' allows for straightforward implementation of the lateral boundary conditions. Impermeable walls enclose the lateral boundaries and the bottom boundary; the normal velocity and the normal CO_2 flux through them are zero. The vanishing normal velocity implies that the normal derivative of Ψ' must be zero along these boundaries. Along the top boundary, $\tilde{\omega}$ is fixed (equal to one) and $\tilde{\omega}' = 0$. We follow earlier papers[27–37] and treat the top

boundary as being impermeable to convection but not diffusion (see Cheng *et al.*[36] for theoretical reasoning behind this condition) so that $\tilde{q}_z = 0$. This implies that Ψ' must be a constant along this boundary. Without loss of generality, we may set the constant equal to zero, since $\tilde{\mathbf{q}}$ is invariant with respect to the value of the constant. The same reasoning is used to justify $\Psi' = 0$ along the bottom. In summary, the stability analysis solves (19) and (20) for the perturbations Ψ' and $\tilde{\omega}'$, with $\tilde{\omega}_{\text{base}}$ given by (17). The boundary conditions in Cartesian geometries are

$$\left.\frac{\partial \Psi'}{\partial \tilde{x}}\right|_{(\tilde{x}=0,\tilde{y},\tilde{z},\tilde{t})} = \left.\frac{\partial \tilde{\omega}'}{\partial \tilde{x}}\right|_{(\tilde{x}=0,\tilde{y},\tilde{z},\tilde{t})} = \left.\frac{\partial \Psi'}{\partial \tilde{x}}\right|_{(\tilde{x}=\tilde{W},\tilde{y},\tilde{z},\tilde{t})} = \left.\frac{\partial \tilde{\omega}'}{\partial \tilde{x}}\right|_{(\tilde{x}=\tilde{W},\tilde{y},\tilde{z},\tilde{t})} = 0, \quad \forall \tilde{y}, \tilde{z}, \tilde{t}, \tag{21}$$

$$\left.\frac{\partial \Psi'}{\partial \tilde{y}}\right|_{(\tilde{x},\tilde{y}=0,\tilde{z},\tilde{t})} = \left.\frac{\partial \tilde{\omega}'}{\partial \tilde{y}}\right|_{(\tilde{x},\tilde{y}=0,\tilde{z},\tilde{t})} = \left.\frac{\partial \Psi'}{\partial \tilde{y}}\right|_{(\tilde{x},\tilde{y}=A\tilde{W},\tilde{z},\tilde{t})} = \left.\frac{\partial \tilde{\omega}'}{\partial \tilde{y}}\right|_{(\tilde{x},\tilde{y}=A\tilde{W},\tilde{z},\tilde{t})} = 0, \quad \forall \tilde{x}, \tilde{z}, \tilde{t}, \tag{22}$$

$$\Psi'(\tilde{x}, \tilde{y}, \tilde{z} = -\mathrm{Ra}, \tilde{t}) = \left.\frac{\partial \tilde{\omega}'}{\partial \tilde{z}}\right|_{(\tilde{x},\tilde{y},\tilde{z}=-\mathrm{Ra},\tilde{t})} = 0, \quad \forall \tilde{x}, \tilde{y}, \tilde{t}, \tag{23}$$

$$\Psi'(\tilde{x}, \tilde{y}, \tilde{z} = 0, \tilde{t}) = \tilde{\omega}'(\tilde{x}, \tilde{y}, \tilde{z} = 0, \tilde{t}) = 0, \quad \forall \tilde{x}, \tilde{y}, \tilde{t}. \tag{24}$$

The boundary conditions in cylindrical geometries are

$$\exists M \in \mathbb{R} \text{ such that } |\Psi'(\tilde{r} = 0, \theta, \tilde{z}, \tilde{t})| \le M, \quad |\tilde{\omega}'(\tilde{r} = 0, \theta, \tilde{z}, \tilde{t})| \le M, \quad \forall \theta, \tilde{z}, \tilde{t}, \tag{25}$$

$$\left.\frac{\partial \Psi'}{\partial \tilde{r}}\right|_{(\tilde{r}=\tilde{R},\theta,\tilde{z},\tilde{t})} = \left.\frac{\partial \tilde{\omega}'}{\partial \tilde{r}}\right|_{(\tilde{r}=\tilde{R},\theta,\tilde{z},\tilde{t})} = 0, \quad \forall \theta, \tilde{z}, \tilde{t}, \tag{26}$$

$$\Psi'(\tilde{r}, \theta, \tilde{z}, \tilde{t}) = \Psi'(\tilde{r}, \theta + 2\pi, \tilde{z}, \tilde{t}), \quad \tilde{\omega}'(\tilde{r}, \theta, \tilde{z}, \tilde{t}) = \tilde{\omega}'(\tilde{r}, \theta + 2\pi, \tilde{z}, \tilde{t}), \quad \forall \tilde{r}, \theta, \tilde{z}, \tilde{t}, \tag{27}$$

$$\Psi'(\tilde{r}, \theta, \tilde{z} = -\mathrm{Ra}, \tilde{t}) = \left.\frac{\partial \tilde{\omega}'}{\partial \tilde{z}}\right|_{(\tilde{r},\theta,\tilde{z}=-\mathrm{Ra},\tilde{t})} = 0, \quad \forall \tilde{r}, \theta, \tilde{t}, \tag{28}$$

$$\Psi'(\tilde{r}, \theta, \tilde{z} = 0, \tilde{t}) = \tilde{\omega}'(\tilde{r}, \theta, \tilde{z} = 0, \tilde{t}) = 0, \quad \forall \tilde{r}, \theta, \tilde{t}. \tag{29}$$

The perturbations Ψ' and $\tilde{\omega}'$ must be bounded at the center, as stated in (25).

B. Solution to the linearized perturbation equations

If the horizontal dimensions are infinite in extent, we may follow earlier studies[27–33,35–37] and express the perturbations $\Psi'(\tilde{x}, \tilde{y}, \tilde{z}, \tilde{t})$ and $\tilde{\omega}'(\tilde{x}, \tilde{y}, \tilde{z}, \tilde{t})$ in terms of Fourier transforms

$$\Psi'(\tilde{x}, \tilde{y}, \tilde{z}, \tilde{t}) = \frac{1}{4\pi^2} \int_{-\infty}^{+\infty} \int_{-\infty}^{+\infty} \hat{\Psi}'(\tilde{s}_x, \tilde{s}_y, \tilde{z}, \tilde{t}) \exp\left[\sqrt{-1}\left(\tilde{s}_x \tilde{x} + \tilde{s}_y \tilde{y}\right)\right] \mathrm{d}\tilde{s}_x \mathrm{d}\tilde{s}_y, \tag{30}$$

$$\tilde{\omega}'(\tilde{x}, \tilde{y}, \tilde{z}, \tilde{t}) = \frac{1}{4\pi^2} \int_{-\infty}^{+\infty} \int_{-\infty}^{+\infty} \hat{\omega}'(\tilde{s}_x, \tilde{s}_y, \tilde{z}, \tilde{t}) \exp\left[\sqrt{-1}\left(\tilde{s}_x \tilde{x} + \tilde{s}_y \tilde{y}\right)\right] \mathrm{d}\tilde{s}_x \mathrm{d}\tilde{s}_y, \tag{31}$$

where $\tilde{s}_x$ and $\tilde{s}_y$ are the dimensionless wavenumbers in $\tilde{x}$ and $\tilde{y}$, respectively. Let us define a wavenumber

$$\tilde{s}_f = \sqrt{\tilde{s}_x^2 + \tilde{s}_y^2}. \tag{32}$$

The only requirement on $\tilde{s}_f$ is that it must be positive in order for it to be physically meaningful. Substituting (30) and (31) into (19) and (20), we obtain

$$\frac{\partial \hat{\omega}'}{\partial \tilde{t}} = -\tilde{s}_f^2 \hat{\Psi}' \frac{\partial \tilde{\omega}_{\text{base}}}{\partial \tilde{z}} + \left(\frac{\partial^2}{\partial \tilde{z}^2} - \tilde{s}_f^2 \right) \hat{\omega}', \tag{33}$$

$$\left(\frac{\partial^2}{\partial \tilde{z}^2} - \tilde{s}_f^2 \right) \hat{\Psi}' = \hat{\omega}'. \tag{34}$$

For confined Cartesian geometries, the lateral boundary conditions (21) and (22) are satisfied if we represent Ψ' and $\tilde{\omega}'$ in series expansions

$$\Psi'(\tilde{x}, \tilde{y}, \tilde{z}, \tilde{t}) = \sum_{i=0}^{\infty} \sum_{j=0}^{\infty} \hat{\Psi}'(\tilde{s}_{ij}, \tilde{z}, \tilde{t}) \cos\left(\frac{i\pi \tilde{x}}{\tilde{W}} \right) \cos\left(\frac{j\pi \tilde{y}}{A\tilde{W}} \right), \tag{35}$$

$$\tilde{\omega}'(\tilde{x}, \tilde{y}, \tilde{z}, \tilde{t}) = \sum_{i=0}^{\infty} \sum_{j=0}^{\infty} \hat{\omega}'(\tilde{s}_{ij}, \tilde{z}, \tilde{t}) \cos\left(\frac{i\pi \tilde{x}}{\tilde{W}} \right) \cos\left(\frac{j\pi \tilde{y}}{A\tilde{W}} \right), \tag{36}$$

where the wavenumber $\tilde{s}_{ij}$, which is required to be positive, is

$$\tilde{s}_{ij} = \frac{\pi \sqrt{i^2 + (j/A)^2}}{\tilde{W}}. \tag{37}$$

Substituting (35) and (36) into (19) and (20) gives

$$\frac{\partial \hat{\omega}'}{\partial \tilde{t}} = -\tilde{s}_{ij}^2 \hat{\Psi}' \frac{\partial \tilde{\omega}_{\text{base}}}{\partial \tilde{z}} + \left(\frac{\partial^2}{\partial \tilde{z}^2} - \tilde{s}_{ij}^2 \right) \hat{\omega}', \tag{38}$$

$$\left(\frac{\partial^2}{\partial \tilde{z}^2} - \tilde{s}_{ij}^2 \right) \hat{\Psi}' = \hat{\omega}'. \tag{39}$$

Comparing (38) and (39) with (33) and (34), it is evident that the lateral boundaries affect the results by allowing only perturbation modes with wavenumbers of the form (37) to develop. The base state may be significantly more stable (the onset of convection delayed) in a confined domain if modes similar to the earliest-growing one cannot be admitted.

We apply the same eigenfunction expansion approach to simplify (19) and (20) in cylindrical coordinates. The radial dependence of Ψ' and $\tilde{\omega}'$ is expressed in terms of Bessel functions of the first kind, which are eigenfunctions of the radial part of the Laplacian.[53] The boundary condition (25) precludes the use of Bessel functions of the second kind, since these functions become unbounded as their argument approaches zero.[54] The Bessel function of order m is denoted as $J_m(\tilde{s}_{lm}\tilde{r})$ and is the solution to

$$\left[\frac{\mathrm{d}^2}{\mathrm{d}\tilde{r}^2} + \frac{1}{\tilde{r}} \frac{\mathrm{d}}{\mathrm{d}\tilde{r}} + \left(\tilde{s}_{lm}^2 - \frac{m^2}{\tilde{r}^2} \right) \right] J_m(\tilde{s}_{lm}\tilde{r}) = 0, \tag{40}$$

where the wavenumber $\tilde{s}_{lm}$ is

$$\tilde{s}_{lm} = \frac{b_{lm}}{\tilde{R}}. \tag{41}$$

Only positive values of $\tilde{s}_{lm}$ that satisfy (26) are allowed. Thus, b_{lm} represents the positive zeros of $\mathrm{d}J_m(\tilde{s}_{lm}\tilde{r})/\mathrm{d}\tilde{r}$ for $\tilde{r} = \tilde{R}$. Each Bessel function J_m has an infinite number of possible values of $\tilde{s}_{lm}$ that satisfy (26); we use the index l to keep track of each value. We may represent Ψ' and $\tilde{\omega}'$ in series expansions

$$\Psi'(\tilde{r}, \theta, \tilde{z}, \tilde{t}) = \sum_{l=0}^{\infty} \sum_{m=0}^{\infty} \hat{\Psi}'(\tilde{s}_{lm}, \tilde{z}, \tilde{t}) J_m(\tilde{s}_{lm}\tilde{r}) \cos(m\theta), \tag{42}$$

$$\tilde{\omega}'(\tilde{r}, \theta, \tilde{z}, \tilde{t}) = \sum_{l=0}^{\infty} \sum_{m=0}^{\infty} \hat{\omega}'(\tilde{s}_{lm}, \tilde{z}, \tilde{t}) J_m(\tilde{s}_{lm}\tilde{r}) \cos(m\theta). \tag{43}$$

Equations (42) and (43) satisfy the boundary condition (27) because m is an integer. Substituting (42) and (43) into (19) and (20) yields

$$\frac{\partial \hat{\omega}'}{\partial \tilde{t}} = -\tilde{s}_{lm}^2 \hat{\Psi}' \frac{\partial \tilde{\omega}_{\text{base}}}{\partial \tilde{z}} + \left(\frac{\partial^2}{\partial \tilde{z}^2} - \tilde{s}_{lm}^2 \right) \hat{\omega}', \tag{44}$$

$$\left(\frac{\partial^2}{\partial \tilde{z}^2} - \tilde{s}_{lm}^2 \right) \hat{\Psi}' = \hat{\omega}'. \tag{45}$$

We mentioned in Sec. I that Kim *et al.*[34] have studied the effect of lateral boundaries in cylindrical domains for the transient base state problem. In their analysis, the perturbations are required to have a vanishing radial derivative at the center, which implies that the derivative of the Bessel functions must be zero at $\tilde{r} = 0$. This requirement excludes the $m = 1$ solution, because $\mathrm{d}J_1(0)/\mathrm{d}\tilde{r} \neq 0$. Bessel functions with $m \neq 1$ are allowed, however. We show in Sec. IV A that the $m = 1$ solution is the earliest-growing mode in some cases. Thus, Kim *et al.*[34] impose boundary conditions that may artificially stabilize the base state.

The three sets of coupled partial differential equations (33)–(34), (38)–(39), and (44)–(45) closely resemble each other, with the only difference being in the allowable perturbation modes. All three sets may be solved using the method described in earlier papers.[28,29,31,33,35,36] In this method, we expand $\hat{\Psi}'$ and $\hat{\omega}'$ in Fourier series that take into account the boundary conditions (23) and (28) at $\tilde{z} = -\mathrm{Ra}$ and (24), (29) at $\tilde{z} = 0$,

$$\hat{\Psi}'(\tilde{s}, \tilde{z}, \tilde{t}) \approx \sum_{n=1}^{N} \hat{\Psi}'_n(\tilde{s}, \tilde{t}) \sin\left(n\pi \frac{\tilde{z}}{\mathrm{Ra}} \right), \tag{46}$$

$$\hat{\omega}'(\tilde{s}, \tilde{z}, \tilde{t}) \approx \sum_{n=1}^{N} \hat{\omega}'_n(\tilde{s}, \tilde{t}) \sin\left[\left(n - \frac{1}{2} \right) \pi \frac{\tilde{z}}{\mathrm{Ra}} \right], \tag{47}$$

where N is a sufficiently large integer and $\tilde{s}$ could represent $\tilde{s}_f$, $\tilde{s}_{ij}$, or $\tilde{s}_{lm}$. We substitute (46) and (47) into (33)–(34), (38)–(39), and (44)–(45), multiply the equations by a complementary set of orthogonal (sinusoidal) functions, and integrate over the spatial coordinate $\tilde{z}$ to eliminate the dependence on $\tilde{z}$. Performing this sequence of steps transforms the coupled partial differential equations into a system of ordinary differential equations

$$\frac{\mathrm{d}\boldsymbol{\omega}}{\mathrm{d}\tilde{t}} = \mathbf{A}\boldsymbol{\omega}, \tag{48}$$

where $\boldsymbol{\omega}$ is the column vector $\left(\hat{\omega}'_1, \hat{\omega}'_2, ..., \hat{\omega}'_N \right)^T$, and $\mathbf{A}$ is the time-dependent real matrix derived in earlier works.[28,29,31,33,35,36] This matrix depends on time $\tilde{t}$ and on the wavenumber $\tilde{s}$. Before the onset of convection, all perturbation modes decay with time because they are dissipated by diffusion. We define the critical time to be the earliest instance (the minimum time over all wavenumbers) when a perturbation mode begins to grow. This is equivalent to the first instance when the most positive eigenvalue of $\mathbf{A} + \mathbf{A}^T$ becomes greater than zero.[35,36] This eigenvalue, which we denote as σ, represents the largest instantaneous growth rate of a particular mode. The wavenumber of the earliest-growing mode is the critical wavenumber. To find the critical time and critical wavenumber, we compute σ for many points in wavenumber–time space, i.e., the space of possible values for $\tilde{s}$ and $\tilde{t}$.

III. THE CRITICAL TIME AND THE CRITICAL WAVENUMBER

A. Unconfined domains

The base state is most unstable in an unconfined domain because all perturbation modes, including the earliest-growing one, are allowed when the horizontal dimensions are infinitely large. For an unconfined domain, we label the critical time as $\tilde{t}_c$ and the critical wavenumber as $\tilde{s}_c$.

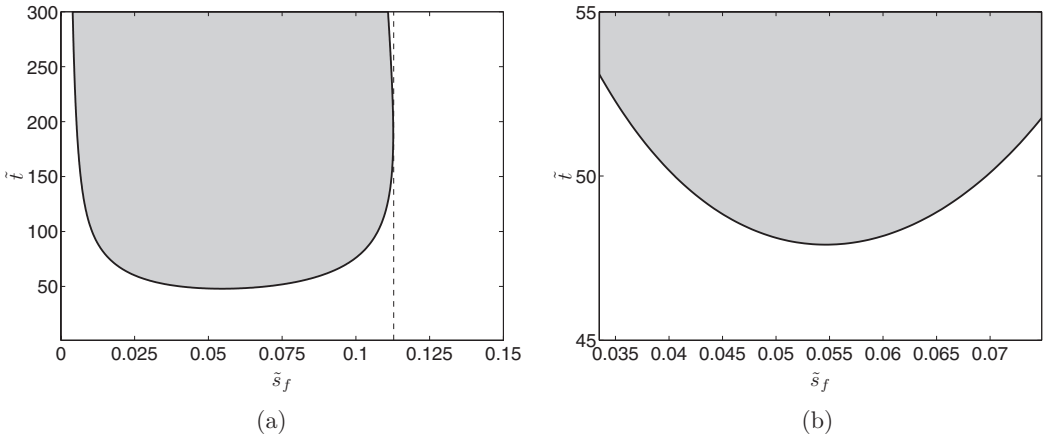

FIG. 1. (a) Marginal stability ($\sigma = 0$) contour in dimensionless wavenumber–time space in an unconfined domain; (b) zoomed-in view around the critical time $\tilde{t}_c \approx 47.9$ and critical wavenumber $\tilde{s}_c \approx 0.0545$. The base state is unstable in the shaded region above the contour and is stable under it. The dashed line represents the large wavenumber cutoff of $\tilde{s}_f \approx 2.07\tilde{s}_c \approx 0.113$. Perturbation modes with wavenumbers larger than this cutoff do not become unstable.

Previous studies[35,36] have found that $\tilde{t}_c \approx 47.9$ and $\tilde{s}_c \approx 0.0545$. Figure 1 depicts the $\sigma = 0$ contour in wavenumber–time space. This contour represents states of marginal stability, because the base state is unstable in the shaded region above the contour ($\sigma > 0$ and the onset of convection has occurred) and is stable under it. The figure reveals two key features. First, there is a large wavenumber cutoff of $\tilde{s}_f \approx 2.07\tilde{s}_c \approx 0.113$, which is represented by the dashed line. Perturbation modes with wavenumbers larger than this cutoff do not become unstable. We show in Secs. III B–III C that convection cannot occur in confined domains where the wavenumbers are restricted to be larger than this cutoff. There is also a small wavenumber cutoff, but this limit is not important for our work. Convection may occur for only an intermediate range of wavenumbers because diffusion strongly dissipates perturbation modes at the two extremes. More details on the diffusive dissipation may be found in our earlier paper.[36] The second key feature from Figure 1 is that many modes with wavenumbers close to $\tilde{s}_c$ are nearly degenerate in the sense that they become unstable at almost the same time. Modes that are within roughly 30% of $\tilde{s}_c$ in either direction become unstable at a time that is still within a few percentage points of $\tilde{t}_c$. Thus, we expect the lateral boundaries to have a much greater effect on the wavenumber of the earliest-growing mode than on the onset time.

B. Cartesian versus cylindrical domains

We now compare the onset of convection in Cartesian versus cylindrical geometries. In confined domains, only perturbation modes with wavenumbers that satisfy the lateral boundary conditions are allowed to develop. In order to quantify how the boundaries affect the results, we analyze how closely the allowable wavenumbers converge to $\tilde{s}_c$ as a function of the dimensionless width $\tilde{W}$ or the dimensionless diameter $2\tilde{R}$. Towards this goal, we examine two quantities: (1) a percent difference $|\Delta\tilde{s}|_{\min}$ and (2) a wavenumber $\tilde{s}_{\min}$. The percent difference $|\Delta\tilde{s}|_{\min}$ is defined as

$$|\Delta\tilde{s}|_{\min} = 100 \inf_{\tilde{s}} \frac{|\tilde{s} - \tilde{s}_c|}{\tilde{s}_c}, \tag{49}$$

where $\tilde{s}$ denotes $\tilde{s}_{ij}$ or $\tilde{s}_{lm}$ and inf denotes the infimum (greatest lower bound). The value of $\tilde{s}_{ij}$ or $\tilde{s}_{lm}$ that minimizes the quantity $|\tilde{s} - \tilde{s}_c|$ is $\tilde{s}_{\min}$. We may interpret $\tilde{s}_{\min}$ as the wavenumber of the earliest-growing mode in confined domains (i.e., the analogue to $\tilde{s}_c$). Figure 2 presents the effect of the lateral boundaries on $|\Delta\tilde{s}|_{\min}$ and $\tilde{s}_{\min}$. These quantities are plotted as a function of $2\tilde{R}$ instead of $\tilde{R}$ so that we can more readily compare the behavior in the two geometries. The aspect ratio A is equal to one in Figures 2(a) and 2(c) so that both $\tilde{x}$ and $\tilde{y}$ range from 0 to $\tilde{W}$. We present the effect of varying the aspect ratio in Secs. III C and III D. As expected, the boundaries generally

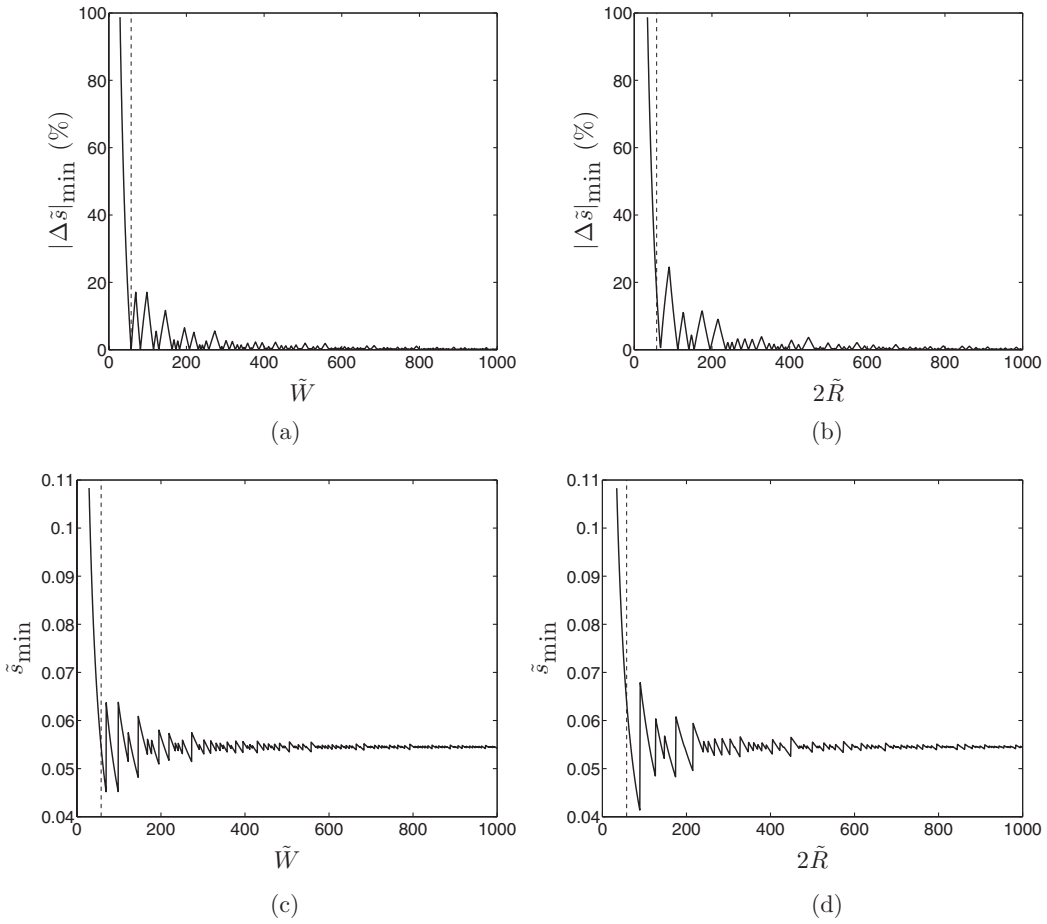

FIG. 2. (a) and (b) $|\Delta\tilde{s}|_{\min}$ vs. $\tilde{W}$ or $2\tilde{R}$; (c) and (d) $\tilde{s}_{\min}$ vs. $\tilde{W}$ or $2\tilde{R}$. The aspect ratio A is unity in (a) and (c) so that both $\tilde{x}$ and $\tilde{y}$ range from 0 to $\tilde{W}$. The dashed line represents $\tilde{W} = \pi/\tilde{s}_c \approx 58$ or $2\tilde{R} = 2b_{01}/\tilde{s}_c \approx 68$. The behavior of the system is very different depending on whether it lies to the left or the right of the dashed line, as we describe in the text.

have a greater influence when $\tilde{W}$ or $2\tilde{R}$ is small. In Cartesian geometries, we see from (37) that the smallest wavenumber possible when $A = 1$ is $\pi/\tilde{W}$. In order for a mode with a wavenumber of $\tilde{s}_c$ to develop, $\tilde{W}$ must be at least as large as $\pi/\tilde{s}_c \approx 58$. This is equal to half of a quantity called the critical wavelength[27–37] $\tilde{\lambda}_c$, which is defined as $\tilde{\lambda}_c = 2\pi/\tilde{s}_c$. In cylindrical geometries, the smallest positive value[53,54] that b_{lm} in Eq. (41) can assume is the first zero (the one that corresponds to $l = 0$) of the derivative of the Bessel function J_1. Thus, $2\tilde{R}$ must be at least $2b_{01}/\tilde{s}_c \approx 2(1.8412)/\tilde{s}_c \approx 68$ for a mode with a wavenumber of $\tilde{s}_c$ to develop. The dashed line in Figure 2 represents $\tilde{W} = \pi/\tilde{s}_c$ or $2\tilde{R} = 2b_{01}/\tilde{s}_c$. The behavior of the system is very different depending on whether it lies to the left or the right of the dashed line.

To the right of the dashed line, $\tilde{s}_{\min}$ fluctuates about $\tilde{s}_c$ and converges to $\tilde{s}_c$ as the size of the domain increases. The convergence reflects the fact that the confinement effect becomes negligible in the limit of a large domain. The fluctuations occur because of the following reasons. In Cartesian geometries, we have $\tilde{s}_{\min} = \tilde{s}_c$ (or equivalently, $|\Delta\tilde{s}|_{\min} = 0\%$) when $\tilde{W}$ is of the form $\sqrt{i^2 + j^2}\,(\pi/\tilde{s}_c)$, for $i, j \in \mathbb{N}$. When $\tilde{W}$ is not of this form, $\tilde{s}_{\min} \neq \tilde{s}_c$ and $|\Delta\tilde{s}|_{\min} > 0\%$. Similarly, $\tilde{s}_{\min} = \tilde{s}_c$ only when $2\tilde{R}$ in cylindrical geometries is of the form $2b_{lm}/\tilde{s}_c$. The influence of the lateral boundaries is more pronounced in cylindrical geometries. The largest $|\Delta\tilde{s}|_{\min}$ is about 25% in Figure 2(b), whereas it is 17% in Figure 2(a). Nevertheless, the boundaries have little effect on the onset time for domains that lie to the right of the dashed line. Even if $|\Delta\tilde{s}|_{\min} = 25\%$, the earliest-growing mode becomes unstable at a time that is only slightly later than $\tilde{t}_c$, as we discussed in Sec. III A.

The effect on the onset time may be appreciable when $\tilde{W} < \pi/\tilde{s}_c$ or $2\tilde{R} < 2b_{01}/\tilde{s}_c$. To the left of the dashed line in Figure 2, $\tilde{s}_{min}$ rapidly increases to the large wavenumber cutoff value of $2.07\tilde{s}_c \approx 0.113$. Thus, the onset of convection may be significantly delayed. In fact, $\tilde{s}_{min}$ cannot be smaller than the cutoff when $\tilde{W} < (1/2.07)\pi/\tilde{s}_c \approx 28$ or $2\tilde{R} < (2/2.07)b_{01}/\tilde{s}_c \approx 33$. Convection cannot even occur in domains smaller than these limits. The lateral boundaries have a more pronounced effect in smaller cylindrical geometries, just like the case in larger domains. This is why the cutoff is reached at a larger value of $2\tilde{R}$ compared to $\tilde{W}$. Our results are similar to the results from Kim *et al.*,[34] despite the differences between their formulation and ours (see Secs. I and II B). They have found that the lateral boundaries have a negligible effect on the onset time when $2\tilde{R} > 60$ (our value is 68) and that convection cannot occur in domains where $2\tilde{R} < 30$ (our value is 33).

C. Influence of the aspect ratio in Cartesian geometries

In Sec. III B, we considered Cartesian domains where the aspect ratio A is equal to one. We now examine the case of $A \neq 1$. Figure 3 depicts $\tilde{s}_{min}$ vs. $\tilde{W}$ for different values of A. The size in the $\tilde{x}$ direction is $\tilde{W}$, while the size in the $\tilde{y}$ direction is $A\tilde{W}$. As we expect, the confinement effect becomes more severe as the aspect ratio decreases. When $\tilde{W} > \pi/\tilde{s}_c$, the amplitude of the fluctuations about $\tilde{s}_c$ is larger in domains with small aspect ratios. When $\tilde{W} < \pi/\tilde{s}_c$ and $A \leq 1$, $\tilde{s}_{min}$ rapidly increases to the large wavenumber cutoff value of $2.07\tilde{s}_c$. However, when $\tilde{W} < \pi/\tilde{s}_c$ and $A > 1$, $\tilde{s}_{min}$ fluctuates about $\tilde{s}_c$ until $\tilde{W}$ becomes small enough that $\tilde{s}_{min}$ begins to monotonically increase towards $2.07\tilde{s}_c$. We explain these observations from a careful examination of (37). This equation shows that increasing the aspect ratio reduces the discrete character of the wavenumber $\tilde{s}_{ij}$, causing it to behave more like a continuous quantity. In this sense, $\tilde{s}_{ij}$ can be more finely tuned in domains where A is large, so that it is easier to attain a value of $\tilde{s}_{min}$ that is similar to $\tilde{s}_c$. Figure 3 shows that for larger aspect ratios, $\tilde{s}_{min} = \tilde{s}_c$ is achieved more frequently (i.e., $\tilde{s}_{min} = \tilde{s}_c$ occurs at more values of $\tilde{W}$). This is because $\tilde{s}_{min} = \tilde{s}_c$ when $\tilde{W}$ can be expressed in the form $\sqrt{i^2 + (j/A)^2}\,(\pi/\tilde{s}_c)$. In domains where $A \leq 1$, the smallest wavenumber possible from (37) is $\pi/\tilde{W}$, so that $\tilde{W}$ must be at least as large as $\pi/\tilde{s}_c$ in order for a mode with a wavenumber of $\tilde{s}_c$ to develop. When $\tilde{W}$ is less than this value [to the left of the dashed line in Figures 3(d)–3(f)], $\tilde{s}_{min}$ increases to $2.07\tilde{s}_c$. However, in domains where $A > 1$, $\tilde{s}_{min}$ increases to $2.07\tilde{s}_c$ only when $\tilde{W}$ is less than $\pi/(A\tilde{s}_c)$. Between $\tilde{W} = \pi/(A\tilde{s}_c)$ and $\tilde{W} = \pi/\tilde{s}_c$ in Figures 3(a)–3(c), $\tilde{s}_{min}$ fluctuates about $\tilde{s}_c$ and is equal to $\tilde{s}_c$ when $\tilde{W} = j\pi/(A\tilde{s}_c)$. Convection may occur in domains where $A > 1$ as long as $\tilde{W} > (1/2.07)\pi/(A\tilde{s}_c)$; this limit is the width at which $\tilde{s}_{min} = 2.07\tilde{s}_c$. Thus, if A is large, it is possible for convection to occur even when one dimension is very small in size. We conclude from this section that large aspect ratios can significantly reduce boundary effects for both small and large values of $\tilde{W}$.

D. Laboratory-scale experiments and numerical simulations

Our stability analysis helps with the interpretation of laboratory-scale experiments conducted in isothermal diffusion-convection cells.[47–49] In the experiments, CO_2 is dissolved into a water-saturated sand column (or an analogous permeable medium such as a Hele-Shaw cell) that resides in the cell, which is cylindrical[47,49] or rectangular[48] in shape. The diameter of the cell is 0.007 m and 0.032 m in Farajzadeh *et al.*[47] and Nazari Moghaddam *et al.*,[49] respectively. The horizontal dimensions of the Hele-Shaw cell in Kneafsey and Pruess[48] are 0.24 m and 0.0024 m. These experimental studies have used artificial porous media where the permeability k is extremely high (estimated to be over 1000 darcy). We can perform a simple calculation to demonstrate that high permeabilities may be necessary in laboratory-scale domains for boundary effects to be negligible. For our calculation, we consider a representative set of conditions where $D = 2 \times 10^{-9}$ m^2/s, $\phi = 0.2$, $\mu = 0.001$ Pa s, $k = 1$ darcy, and $\Delta\rho = 15$ kg/m^3, for which the length scale is $\ell = (D\phi\mu)/(k\Delta\rho g) \approx 0.00275$ m. Note the inverse relation between k and ℓ. A value of $k = 1$ darcy is on the higher end for conventional saline aquifers, where the permeability is typically less than 0.1 darcy. Our calculation will show that $k = 1$ darcy may not be sufficiently high in some laboratory-scale domains. For the representative conditions above, the diameter $2\tilde{R}$ is approximately

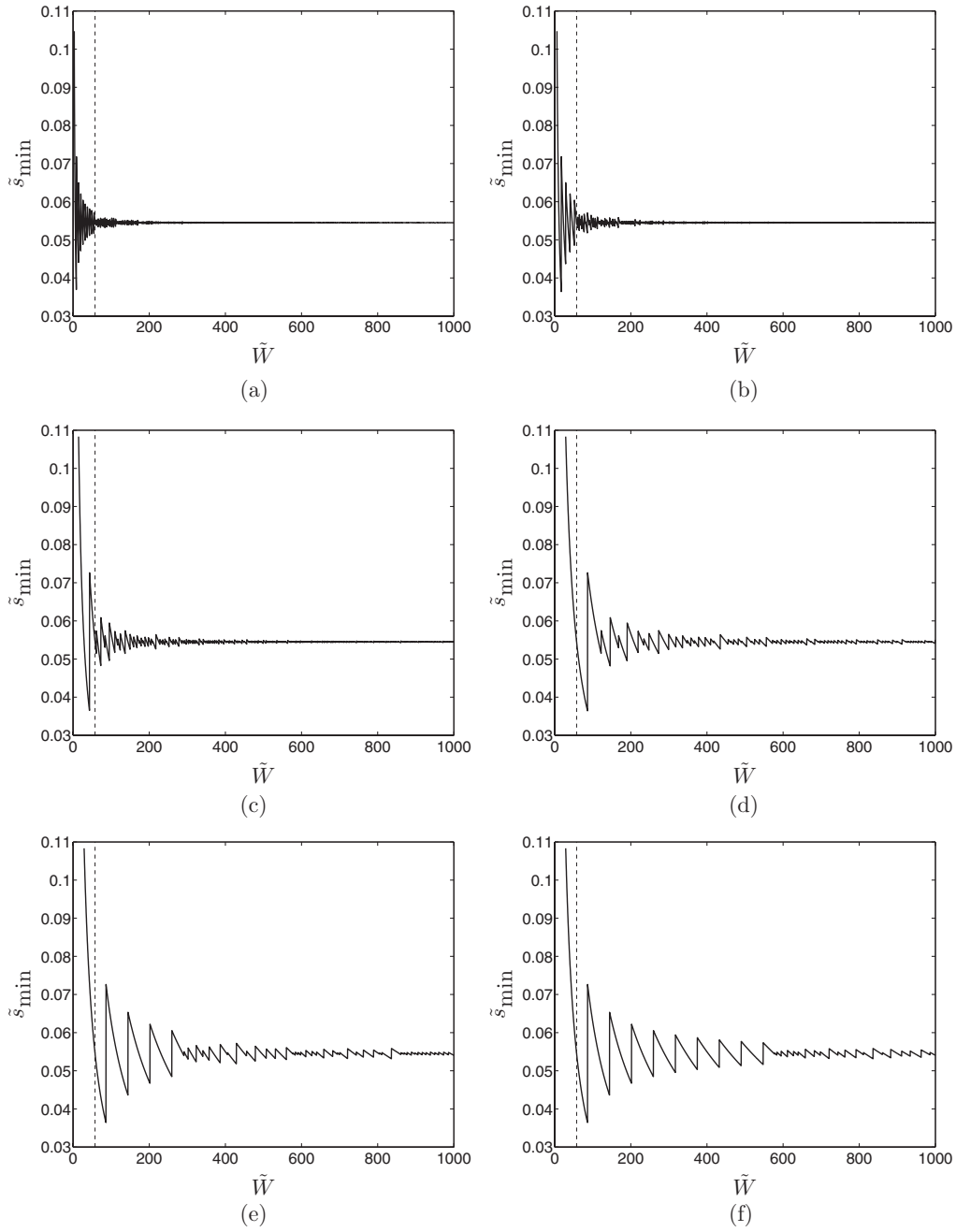

FIG. 3. $\tilde{s}_{\min}$ vs. $\tilde{W}$ for various values of the aspect ratio A: (a) $A = 10$; (b) $A = 5$; (c) $A = 2$; (d) $A = 0.5$; (e) $A = 0.2$; (f) $A = 0.1$. The dashed line represents $\tilde{W} = \pi/\tilde{s}_c$. Large aspect ratios can significantly reduce boundary effects for both small and large values of $\tilde{W}$.

2.5 and 11.6 for Farajzadeh *et al.*[47] and Nazari Moghaddam *et al.*,[49] respectively. Our analysis predicts that the onset of convection cannot occur in these experimental setups, since $2\tilde{R} < 33$. The width $\tilde{W}$ is about 87 for Kneafsey and Pruess,[48] with an aspect ratio of 0.01. Equivalently, their setup could be viewed as one where $\tilde{W} \approx 0.87$ and $A = 100$. In either case, we find that $|\Delta\tilde{s}|_{\min}$ and $\tilde{s}_{\min}$ are about 32.1% and 0.0720, respectively. This $\tilde{s}_{\min}$ leads to an onset time of about 51, which is 6.5% larger than the critical time $\tilde{t}_c \approx 47.9$ in unconfined media. The aspect ratio plays an important role in the Kneafsey and Pruess[48] experiments. If the aspect ratio were equal to one, instead of 100,

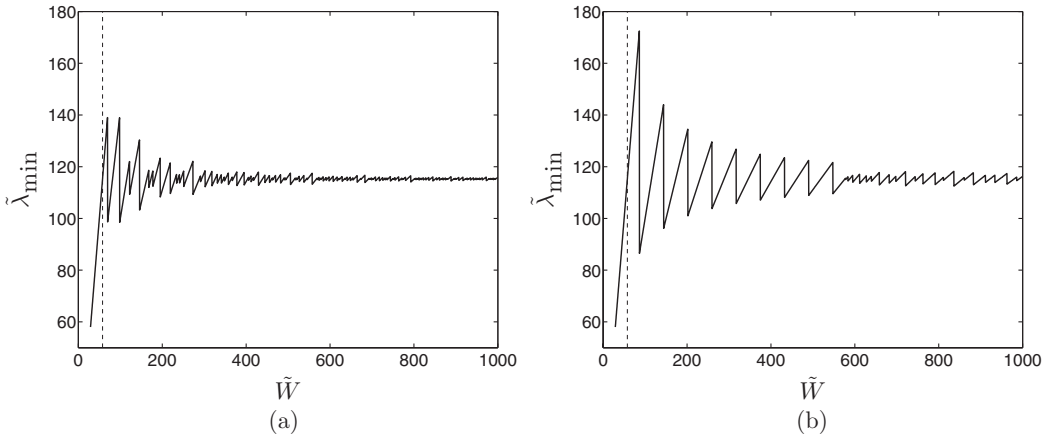

FIG. 4. $\tilde{\lambda}_{\min}$ vs. $\tilde{W}$ in Cartesian geometries at two different aspect ratios: (a) $A = 1$; (b) $A = 0.1$. The dashed line represents $\tilde{W} = \pi/\tilde{s}_c$. Finer gridding in numerical simulations may be necessary to capture the earliest-growing mode in domains where $\tilde{W}$ is small, especially when $A < 1$.

convection would not occur since $\tilde{W} \approx 0.87 < 28$. The lateral boundaries may also affect the onset in natural formations where the permeability is low (a few millidarcy or less). In such formations, the width or diameter may have to be larger than several tens of meters for the boundary effects to be negligible since ℓ would be large. Previous studies emphasize the fact that high permeabilities permit early onset times and strong convective flows. Our work presents a complementary view: high permeabilities minimize confinement effects that impede the onset of convection.

The results may give additional insight into numerical simulations of laboratory-scale or low permeability Cartesian domains where $\tilde{W}$ is small. We define the wavelength of the earliest-growing perturbation mode in confined Cartesian geometries as $\tilde{\lambda}_{\min} = 2\pi/\tilde{s}_{\min}$. The wavelength gives an indication of the size of this mode. Since it is not clear how to define the wavelength in cylindrical geometries, we focus only on Cartesian geometries for this part of our analysis. Figure 4 demonstrates the effect of the boundaries on $\tilde{\lambda}_{\min}$. From the definition of $\tilde{\lambda}_{\min}$, we can see that Figures 4(a) and 4(b) are just "reciprocal mirror images" of Figures 2(c) and 3(f), respectively. The dashed line represents $\tilde{W} = \pi/\tilde{s}_c$. To the right of this line, $\tilde{\lambda}_{\min}$ fluctuates about the critical wavelength $\tilde{\lambda}_c = 2\pi/\tilde{s}_c$ and converges to this value as $\tilde{W}$ increases. To the left of the dashed line, $\tilde{\lambda}_{\min}$ linearly decreases as $\tilde{W}$ becomes smaller. It is important in numerical simulations to use gridding fine enough to capture the earliest-growing mode. This means that the grid spacing must be smaller than $\tilde{\lambda}_{\min}$. Our results suggest that even if all fluid and rock properties are the same as in large domain, finer gridding may be necessary to capture this mode in laboratory-scale or low permeability domains where $\tilde{W}$ is small, especially when $A < 1$.

IV. PATTERNS OF THE EARLIEST-GROWING MODE IN THE HORIZONTAL PLANE

A. Indices of the earliest-growing mode

Equation (37) shows that as $\tilde{W}$ becomes larger, the quantity $\sqrt{i^2 + (j/A)^2}$ must also increase in order for the wavenumber $\tilde{s}_{ij}$ to assume a value of $\tilde{s}_{\min}$ that is close to $\tilde{s}_c$. This means that the indices i and j generally increase with $\tilde{W}$. This trend is illustrated in Figure 5. The figure indicates that as $\tilde{W}$ becomes larger, more terms in the series expansions (35) and (36) for Ψ' and $\tilde{\omega}'$ are generally needed to capture the earliest-growing perturbation mode. Nevertheless, we have found that a relatively small number of terms (i and j less than 200) is sufficient even when $\tilde{W}$ is 1000, a value which is more than eight times larger than the critical wavelength $\tilde{\lambda}_c$ defined in Sec. III B. Figure 5 shows that i increases with $\tilde{W}$ in a discrete stepwise fashion, while j increases in a more continuous manner. Although the transient base state problem is fundamentally different from the Horton-Rogers-Lapwood problem, there are similarities between our results and the results of Beck,[17] who has studied the Horton-Rogers-Lapwood problem in confined Cartesian geometries. Beck reports that when the size in one

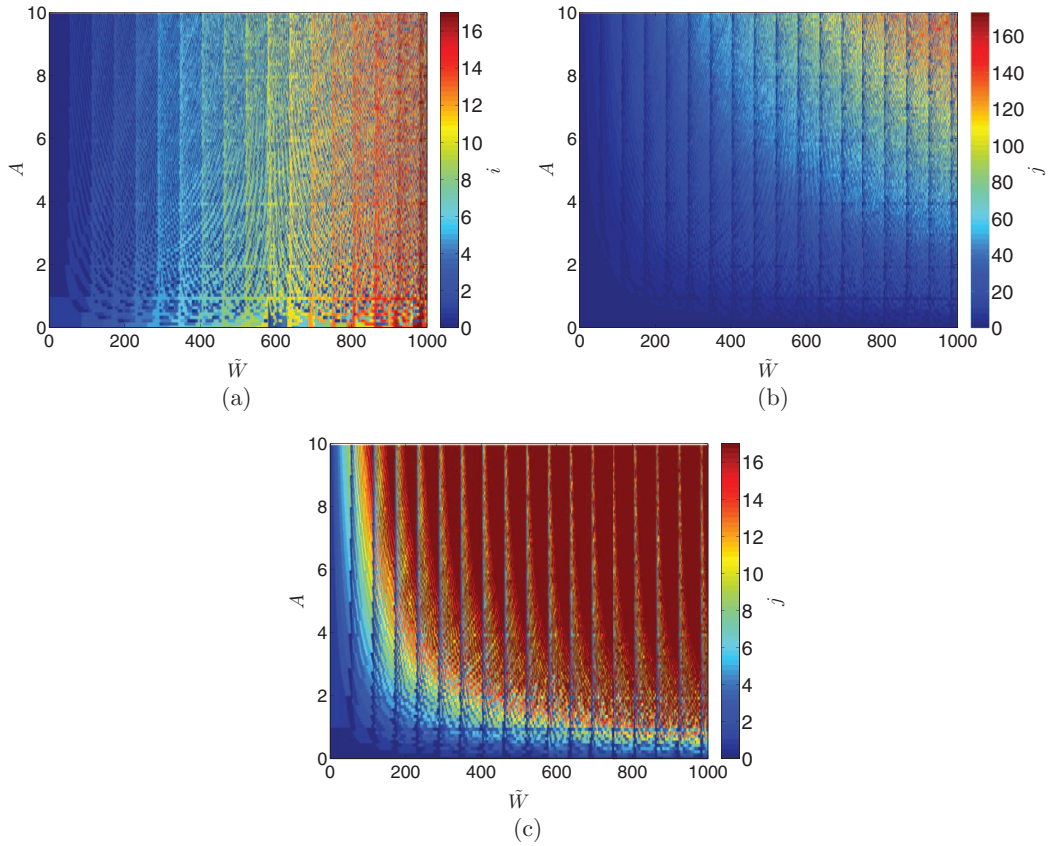

FIG. 5. The indices i and j of the wavenumber $\tilde{s}_{\min}$ of the earliest-growing mode as a function of the width $\tilde{W}$ and the aspect ratio A: (a) the index i in the $\tilde{x}$ direction; (b) the index j in the $\tilde{y}$ direction. The size in this direction ranges from 0 to $A\tilde{W}$; (c) the index j plotted using the same colorbar axis as in (a). The indices generally increase with $\tilde{W}$.

horizontal dimension is small and the size in the other horizontal dimension is much larger, the index in the smaller dimension is zero, while the index in the larger dimension is non-zero. In essence, such geometries prefer modes that are two-dimensional in nature (modes that have a structure in only one horizontal direction as well as the vertical direction). We observe similar results in Figures 5(a) and 5(c). When $A \ll 1$, we have $j = 0$ for most values of $\tilde{W}$, while $i \neq 0$. When $A \gg 1$ and $\tilde{W}$ is small, the earliest-growing mode is characterized by $j \neq 0$ and $i = 0$. In Figure 5(c), there are several vertical lines that are spaced evenly apart from each other. These vertical lines correspond to $\tilde{W}$ that are of the form $i\pi/\tilde{s}_c$. For these values of $\tilde{W}$, we have $\tilde{s}_{\min} = \tilde{s}_c$ and $j = 0$.

Figure 6 shows that like in Cartesian geometries, a relatively small number of terms in the series expansions (42) and (43) is sufficient to capture the earliest-growing mode in cylindrical domains. However, the indices l and m change erratically with the diameter $2\tilde{R}$. This behavior can be understood from an examination of Table I, which shows that some of the zeros of $\mathrm{d}J_{m_1}(\tilde{r})/\mathrm{d}\tilde{r}$ and $\mathrm{d}J_{m_2}(\tilde{r})/\mathrm{d}\tilde{r}$ for $m_1 \neq m_2$ can be close to each other (e.g., b_{50}, b_{52}, and b_{44}). The number of closely matching zeros becomes greater as we consider larger values of l and m; in our study we go up to l, $m = 100$. Thus for a given diameter, there are several Bessel functions (for which the values of m may be very different) that can produce a wavenumber $\tilde{s}_{lm}$ that is close to $\tilde{s}_c$. The earliest-growing mode is usually non-axisymmetric ($m \neq 0$). It is axisymmetric in a few cases. Zebib[19] has also found that the preferred mode for the Horton-Rogers-Lapwood problem in cylindrical geometries is usually non-axisymmetric. The sharp change in m for certain $\tilde{R}$ suggests that adjusting the diameter of the cylinder by a small increment around these $\tilde{R}$ may dramatically alter the patterns of the earliest-growing mode, which we discuss below.

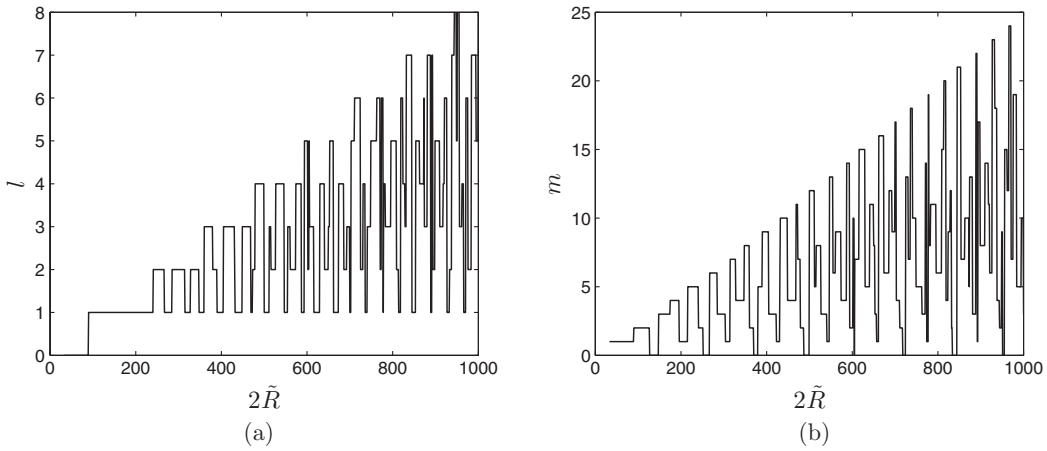

FIG. 6. The indices l and m of the wavenumber $\tilde{s}_{\min}$ of the earliest-growing mode as a function of the diameter $2\tilde{R}$: (a) l; (b) m. The earliest-growing mode is usually non-axisymmetric ($m \neq 0$).

B. Patterns in Cartesian geometries

The patterns of the earliest-growing perturbation mode in the horizontal plane ($\tilde{x}\tilde{y}$ or $\tilde{r}\theta$ plane) reveal many features of the dynamics. In Cartesian domains where $A = 1$, the patterns are symmetric with respect to a reflection across $\tilde{y} = \tilde{x}$ because the solution of the form $\cos(i\pi\tilde{x}/\tilde{W})\cos(j\pi\tilde{y}/\tilde{W})$ is equally unstable with the solution of the form $\cos(j\pi\tilde{x}/\tilde{W})\cos(i\pi\tilde{y}/\tilde{W})$. Therefore, the earliest-growing mode of the perturbations Ψ' and $\tilde{\omega}'$ for $A = 1$ may be expressed, respectively, as

$$\Psi'(\tilde{x}, \tilde{y}, \tilde{z}, \tilde{t}) = \hat{\Psi}'(\tilde{s}_{ij}, \tilde{z}, \tilde{t})\left[\cos\left(\frac{i\pi\tilde{x}}{\tilde{W}}\right)\cos\left(\frac{j\pi\tilde{y}}{\tilde{W}}\right) + \cos\left(\frac{j\pi\tilde{x}}{\tilde{W}}\right)\cos\left(\frac{i\pi\tilde{y}}{\tilde{W}}\right)\right], \tag{50}$$

$$\tilde{\omega}'(\tilde{x}, \tilde{y}, \tilde{z}, \tilde{t}) = \hat{\omega}'(\tilde{s}_{ij}, \tilde{z}, \tilde{t})\left[\cos\left(\frac{i\pi\tilde{x}}{\tilde{W}}\right)\cos\left(\frac{j\pi\tilde{y}}{\tilde{W}}\right) + \cos\left(\frac{j\pi\tilde{x}}{\tilde{W}}\right)\cos\left(\frac{i\pi\tilde{y}}{\tilde{W}}\right)\right], \tag{51}$$

where i and j are the indices of $\tilde{s}_{\min}$ for the corresponding $\tilde{W}$. For simplicity, we may set the Fourier coefficients $\hat{\Psi}' = \hat{\omega}' = 1$. Doing this does not change the appearance of the patterns in the horizontal plane because $\hat{\Psi}'$ and $\hat{\omega}'$ do not depend on $\tilde{x}$ and $\tilde{y}$. Figure 7 shows that the perturbations tend to be highly localized in very positive (red) or very negative (blue) regions. Negative regions are areas where $\Psi = \Psi_{\text{base}} + \Psi' < \Psi_{\text{base}}$ and $\tilde{\omega} = \tilde{\omega}_{\text{base}} + \tilde{\omega}' < \tilde{\omega}_{\text{base}}$. Table II presents the values of i and j used in Figure 7. Except in the special cases where $i = j$ [Figure 7(b)] or one of the indices is equal to zero [Figure 7(c)], there are channels that connect positive regions to each other and other channels that connect negative regions to each other. To the best of our knowledge, patterns in the horizontal plane have not been examined in previous stability analyses of the transient base state problem. We can, however, compare our results with the patterns from Pau *et al.*,[50] who have performed

TABLE I. Zeros (values of b_{lm}) of the Bessel function derivatives $\mathrm{d}J_m(\tilde{r})/\mathrm{d}\tilde{r}$ for $l, m = 0, 1, 2, \ldots, 5$. Note that $\mathrm{d}J_1(0)/\mathrm{d}\tilde{r} \neq 0$. This has implications for Kim *et al.*,[34] as we discussed in Sec. II B.

	$m = 0$	$m = 1$	$m = 2$	$m = 3$	$m = 4$	$m = 5$
$l = 0$	0	1.8412	0	0	0	0
$l = 1$	3.8317	5.3314	3.0542	4.2012	5.3176	6.4156
$l = 2$	7.0156	8.5363	6.7061	8.0152	9.2824	10.5199
$l = 3$	10.1735	11.7060	9.9695	11.3459	12.6819	13.9872
$l = 4$	13.3237	14.8636	13.1704	14.5858	15.9641	17.3128
$l = 5$	16.4706	18.0155	16.3475	17.7887	19.1960	20.5755

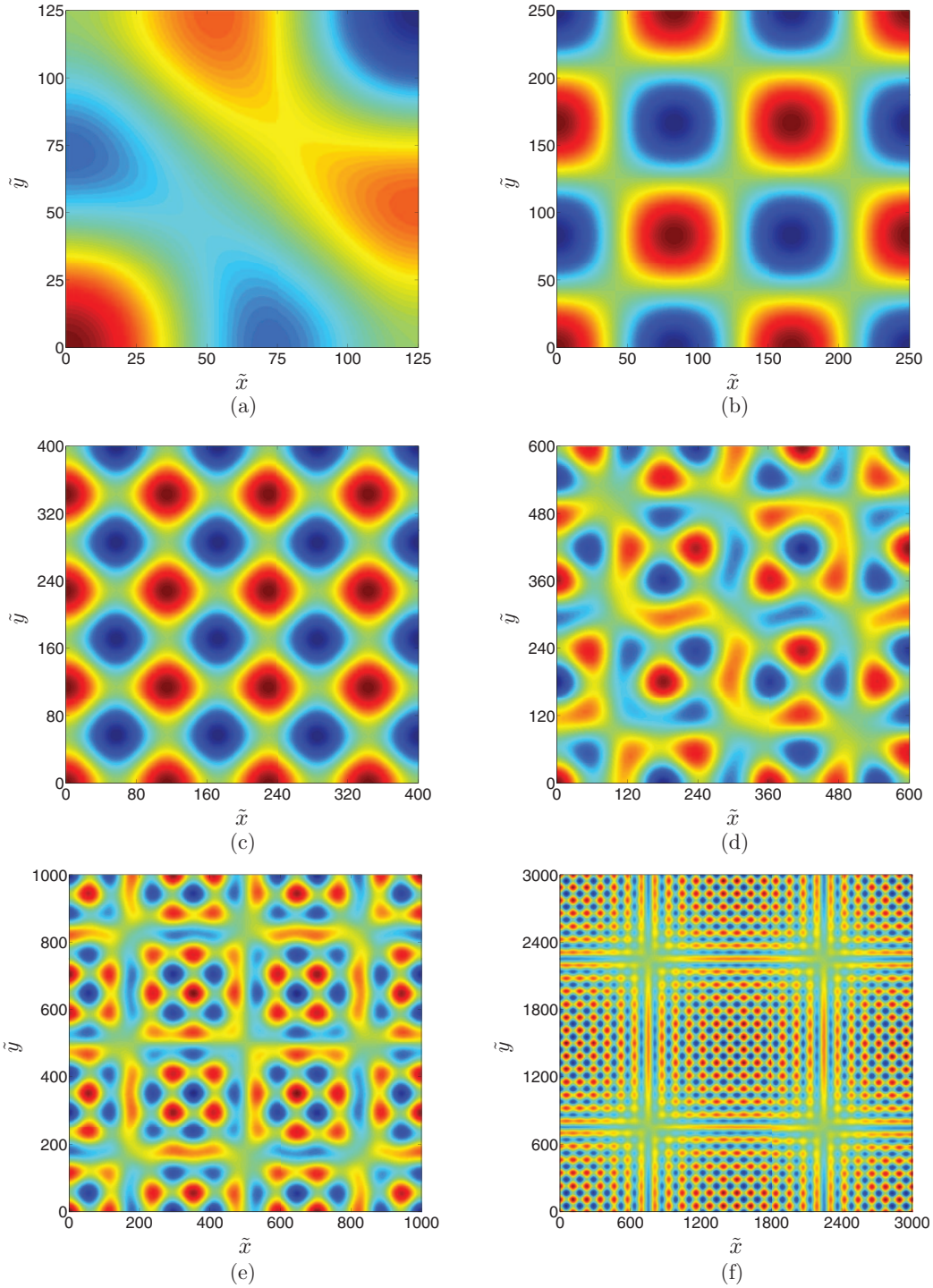

FIG. 7. Patterns in the $\tilde{x}\tilde{y}$ plane of the earliest-growing mode for various $\tilde{W}$ with $A = 1$: (a) $\tilde{W} = 125$; (b) $\tilde{W} = 250$; (c) $\tilde{W} = 400$; (d) $\tilde{W} = 600$; (e) $\tilde{W} = 1000$; (f) $\tilde{W} = 3000$. Perturbations tend to be highly localized in very positive (red) or very negative (blue) regions. In most cases, there are channels that connect positive regions to each other and other channels that connect negative regions to each other. Pau *et al.*[50] have observed similar channels in their numerical simulations.

TABLE II. The indices i and j of $\tilde{s}_{\min}$ for various widths $\tilde{W}$ with $A = 1$.

	$\tilde{W} = 125$	$\tilde{W} = 250$	$\tilde{W} = 400$	$\tilde{W} = 600$	$\tilde{W} = 1000$	$\tilde{W} = 3000$
i	1	3	7	10	17	52
j	2	3	0	3	3	2

three-dimensional numerical simulations of Cartesian geometries. Most simulations of the transient base state problem have been in two-dimensions and are unable to examine the dynamics in the horizontal plane. Pau *et al.*[50] examine patterns *after* the onset of convection, at sufficiently late times when the fluid flow is strong enough to significantly affect the CO_2 dissolution rate into the aqueous phase. Interestingly, Pau *et al.*[50] observe channels for the CO_2 concentration field that are similar to the channels described above. One difference is that their patterns are less ordered (e.g., they are not symmetric with respect to an interchange of $\tilde{x}$ and $\tilde{y}$) because of the nonlinearities that arise after the onset of convection.

Figure 8 illustrates patterns for $\tilde{W} = 400$ at two different aspect ratios: $A = 2$ and $A = 0.5$. The earliest-growing mode when $A = 2$ is of the form $\cos(6\pi\tilde{x}/\tilde{W})\cos[7\pi\tilde{y}/(2\tilde{W})]$, while it is of the form $\cos(7\pi\tilde{x}/\tilde{W})$ when $A = 0.5$ ($j = 0$ for this aspect ratio). Again we set $\hat{\Psi}' = \hat{\omega}' = 1$ so that only the relative (not absolute) difference in Ψ' or $\tilde{\omega}'$ from one region of the plane to another is meaningful. As expected, the patterns are asymmetric with respect to an interchange of $\tilde{x}$ and $\tilde{y}$. This asymmetry allows two-dimensional modes to develop. In fact, as we discussed in Sec. IV A and show in Figure 8(b), two-dimensional modes tend to be preferred when one of the dimensions is small.

C. Patterns in cylindrical geometries

Patterns of the earliest-growing mode in cylindrical geometries are rich in variety, as portrayed in Figures 9 and 10. The earliest-growing mode of the perturbations Ψ' and $\tilde{\omega}'$ are

$$\Psi'(\tilde{r}, \theta, \tilde{z}, \tilde{t}) = \hat{\Psi}'(\tilde{s}_{lm}, \tilde{z}, \tilde{t}) J_m(\tilde{s}_{lm}\tilde{r})\cos(m\theta), \tag{52}$$

$$\tilde{\omega}'(\tilde{r}, \theta, \tilde{z}, \tilde{t}) = \hat{\omega}'(\tilde{s}_{lm}, \tilde{z}, \tilde{t}) J_m(\tilde{s}_{lm}\tilde{r})\cos(m\theta), \tag{53}$$

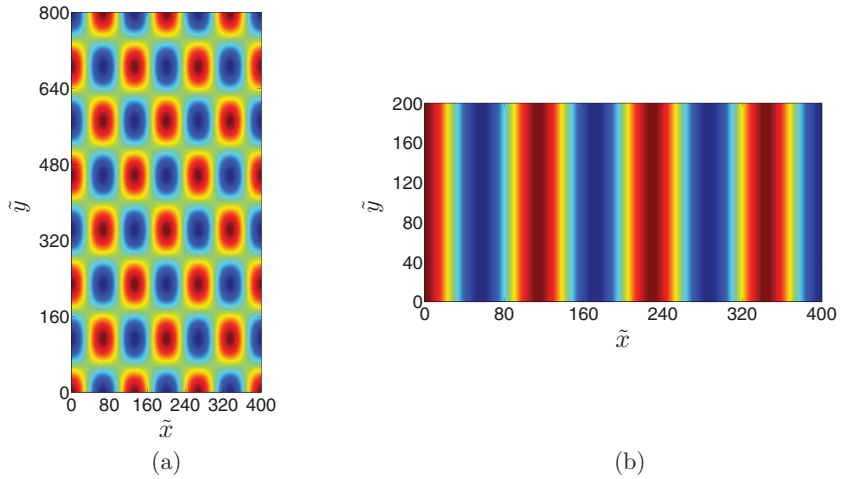

FIG. 8. Patterns in the $\tilde{x}\tilde{y}$ plane of the earliest-growing mode for $\tilde{W} = 400$ at two different aspect ratios: (a) $A = 2$; (b) $A = 0.5$. Patterns are asymmetric with respect to an interchange of $\tilde{x}$ and $\tilde{y}$. Two-dimensional modes tend to be preferred when one of the dimensions is small, as it is in (b).

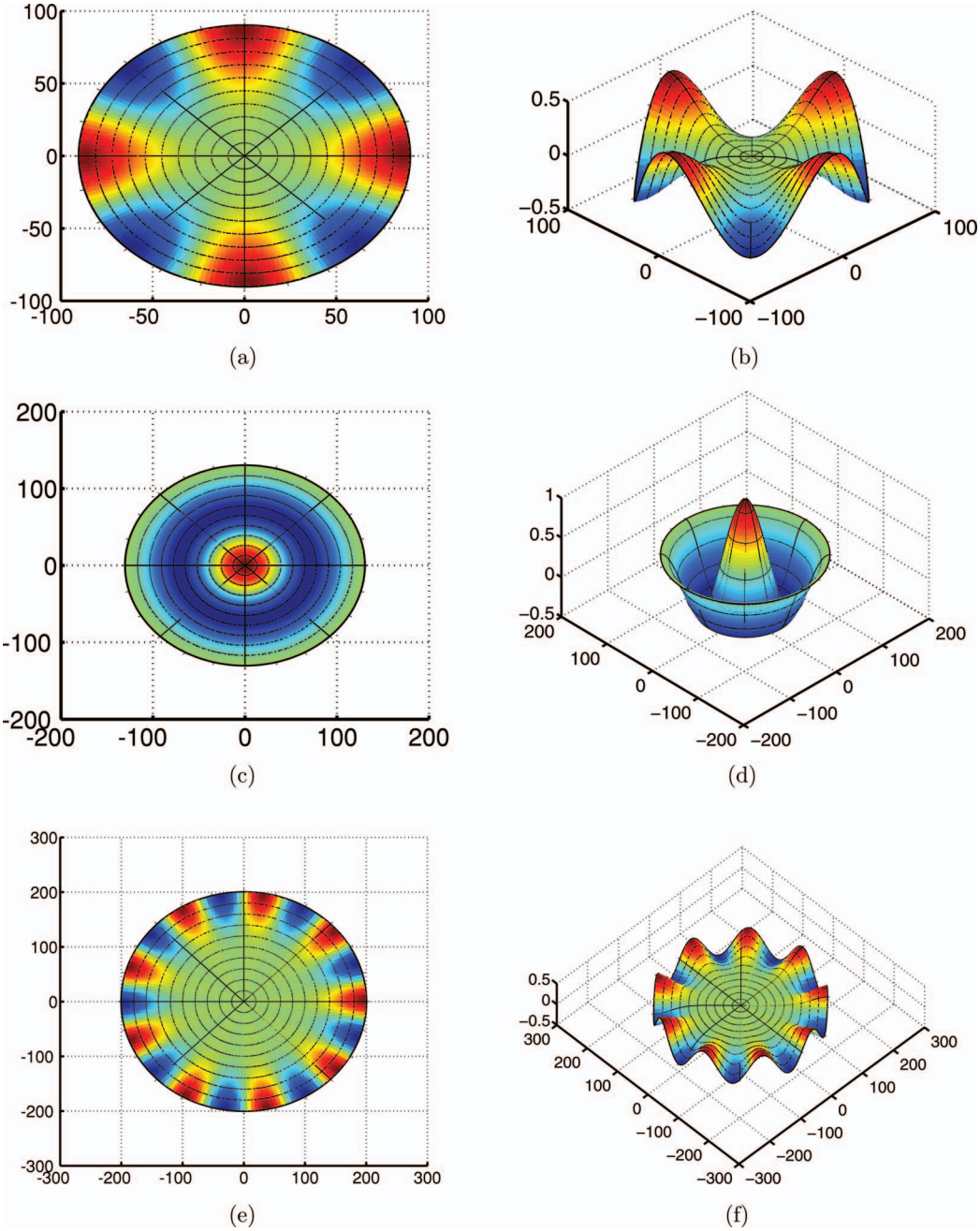

FIG. 9. Top-down and bird's-eye views of patterns in the $\tilde{r}\theta$ plane of the earliest-growing mode for smaller values of $\tilde{R}$ with $\hat{\Psi}' = \hat{\omega}' = 1$: (a), (b) $2\tilde{R} = 180$; (c), (d) $2\tilde{R} = 260$; (e), (f) $2\tilde{R} = 400$.

respectively. The indices l and m of the wavenumber $\tilde{s}_{\min}$ are listed in Table III. The patterns are antisymmetric in the horizontal plane [e.g., $\tilde{\omega}'(\tilde{r}, \theta, \tilde{z}, \tilde{t}) = -\tilde{\omega}'(\tilde{r}, \theta + \pi, \tilde{z}, \tilde{t})$], except when $m = 0$, in which case they are axisymmetric [see Figures 9(c) and 9(d)]. The sinusoidal nature in θ creates alternating positive and negative regions of $\tilde{\omega}'$ or Ψ' that are distinct from the channeling seen in Cartesian geometries. For certain values of $\tilde{R}$, the perturbations are nearly zero (yellowish green) within a large, contiguous circular region around the center. Examples of this type of pattern are shown in Figures 9(a)–9(b), 9(e)–9(f), and 10(e)–10(f). This region near the center may be virtually undisturbed by the earliest-growing mode at early times, which implies that around the onset time,

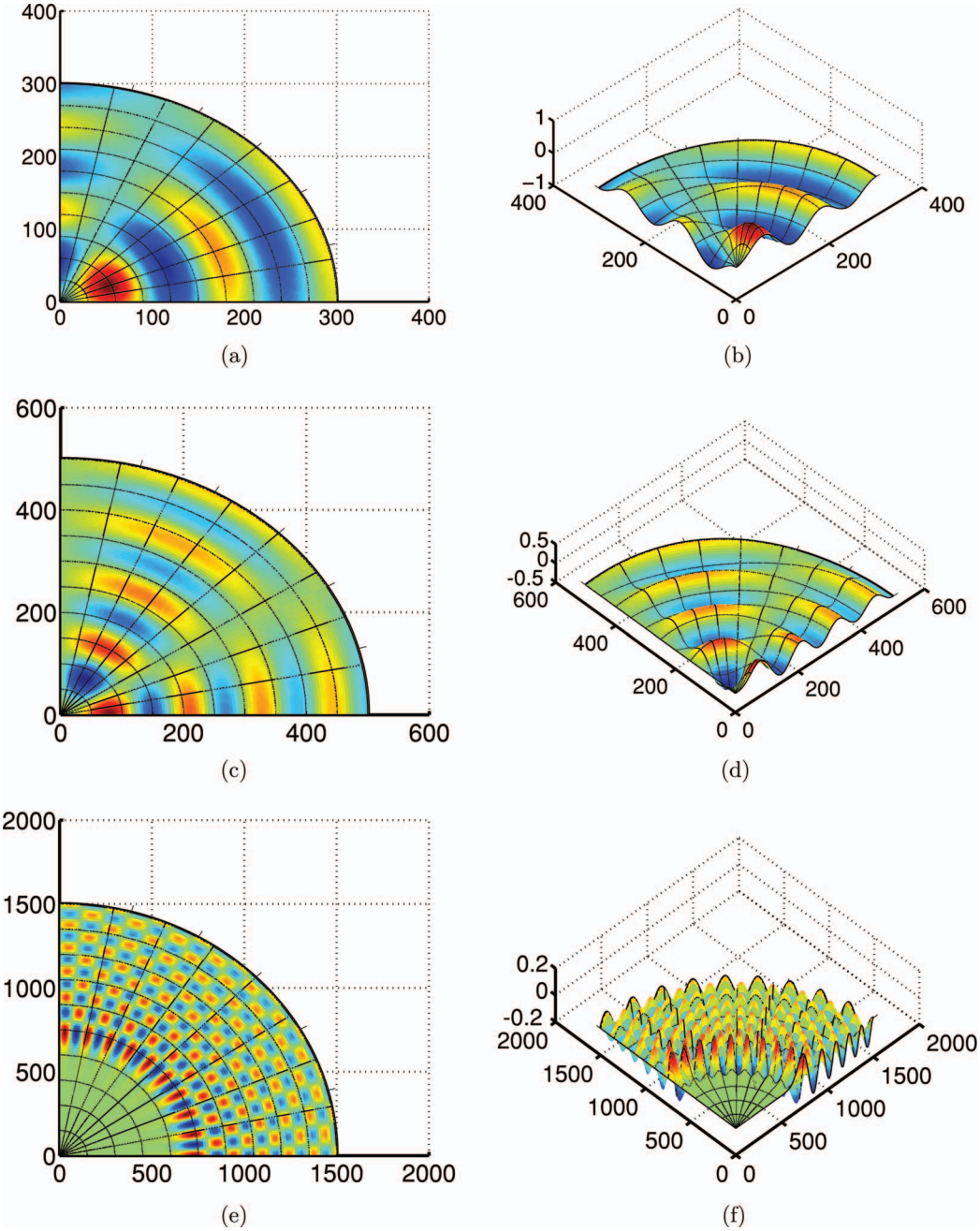

FIG. 10. Top-down and bird's-eye views of patterns in the $\tilde{r}\theta$ plane (for clarity, only one quarter of the plane is shown) of the earliest-growing mode for larger values of $\tilde{R}$ with $\hat{\Psi}' = \hat{\omega}' = 1$: (a), (b) $2\tilde{R} = 600$; (c), (d) $2\tilde{R} = 1000$; (e), (f) $2\tilde{R} = 3000$.

TABLE III. The indices l, m of $\tilde{s}_{\min}$ and the zeros b_{lm} for various diameters $2\tilde{R}$.

	$2\tilde{R} = 180$	$2\tilde{R} = 260$	$2\tilde{R} = 400$	$2\tilde{R} = 600$	$2\tilde{R} = 1000$	$2\tilde{R} = 3000$
l	1	2	1	5	8	11
m	4	0	9	2	3	37
b_{lm}	5.3176	7.0156	10.7114	16.3475	27.3101	81.7936

fluid flow in it may be insignificant compared to the flow in other regions. This is unlike the situation in Cartesian geometries, where the earliest-growing mode acts over the entire domain. Convection may later become significant near the center of the cylinder as the perturbation modes grow with time. We also see that the amplitude and the width of the peaks and valleys decrease in the radial direction. These features result from the spacing of the zeros and other well-known properties of the Bessel functions.[53] These observations indicate that the perturbations are stronger closer to the center, excluding the circular region described above.

D. Cartesian versus cylindrical geometries

The contrasts between the Cartesian and cylindrical patterns may lead to significantly different behavior in the two geometries after the onset time. We hypothesize that the behavior may be different even if the onset time and the wavenumber $\tilde{s}_{\min}$ are the same in both geometries. One important quantity is the CO_2 dissolution rate into the aqueous phase. Pau *et al.*[50] have numerically simulated both two-dimensional (2D) and three-dimensional (3D) Cartesian domains. They report that differences in convection patterns between 2D and 3D translate to a significantly higher CO_2 dissolution rate in 3D after the onset time. This result is observed despite the fact that linear stability analyses predict the same critical time and critical wavenumber in 2D and 3D. Zebib and Kassoy[18] have also discovered that the patterns of the preferred mode can noticeably affect fluid transport rates. They have performed a weakly nonlinear analysis of the Horton-Rogers-Lapwood problem in confined Cartesian geometries. Their analysis shows that three-dimensional perturbation modes (where both $i \neq 0$ and $j \neq 0$) allow considerably more heat transfer than two-dimensional modes when the Rayleigh number is large. The reverse situation is observed for small Rayleigh numbers. Their results are in qualitative agreement with the numerical simulations of Holst and Aziz.[55]

In future studies, we may investigate whether disparate convection patterns in Cartesian and cylindrical geometries persist after the onset time. This may lead to different CO_2 dissolution rates in the two geometries, which could have important implications for sequestration in natural formations and for the interpretation of experiments in laboratory-scale permeable media. Simulations in cylindrical geometries could be compared with the Cartesian geometry results from Pau *et al.*[50] and with our theoretical predictions. Our results in Sec. IV A suggest that a spectral or pseudospectral method may be ideal for solving the Poisson's equation (12) that governs this problem, because a relatively small number of terms in the eigenfunction expansions is sufficient to capture the earliest-growing mode. In addition to comparing the CO_2 dissolution rate, we may examine whether convective flow can be insignificant near the center of the cylinder at early times, as implied by this work.

V. CONCLUSIONS

We have presented a linear stability analysis to determine conditions for the onset of buoyancy-driven convection induced by CO_2 dissolution into water in confined, porous Cartesian and cylindrical geometries. Our problem is characterized by a transient base state. Most stability analyses of the transient base state problem[27–33,35–37] have neglected lateral boundaries and focus on unconfined domains. Kim *et al.*[34] have studied CO_2 dissolution in cylindrical geometries. This article amends their analysis by using more physically realistic boundary conditions and by allowing the perturbations to depend explicitly on time. Our work also considers confined Cartesian geometries where the aspect ratio A between the two horizontal dimensions is not necessarily equal to one, so that the sizes in these directions are $\tilde{W}$ and $A\tilde{W}$. We draw the following conclusions:

- Lateral boundaries impede the onset of convection. The earliest possible onset occurs in unconfined domains at the critical time $\tilde{t}_c \approx 47.9$ with a critical wavenumber $\tilde{s}_c \approx 0.0545$. Perturbation modes with wavenumbers $> 2.07\tilde{s}_c$ do not become unstable.

- When $A > 1$, the lateral boundaries have a negligible effect on the onset time (say, less than 7% larger than $\tilde{t}_c$) if the width $\tilde{W}$ is greater than $\pi/(A\tilde{s}_c)$. Convection cannot occur in domains where $\tilde{W} < (1/2.07)\pi/(A\tilde{s}_c)$. Thus, if A is large, it is possible for convection to occur even when one dimension is very small in size. When $A \leq 1$, these limits become $\pi/\tilde{s}_c \approx 58$ and $(1/2.07)\pi/\tilde{s}_c \approx 28$, respectively.
- The onset time in cylindrical geometries is close to $\tilde{t}_c$ as long as the diameter $2\tilde{R} > 2b_{01}/\tilde{s}_c \approx 68$. Convection cannot occur when $2\tilde{R} < (2/2.07)b_{01}/\tilde{s}_c \approx 33$. These results are similar to those of Kim *et al.*,[34] despite the differences between their formulation and ours. Their values are 60 and 30, respectively.
- The effect on the onset time may be appreciable when $\tilde{W} < \pi/(A\tilde{s}_c)$ (or $\tilde{W} < \pi/\tilde{s}_c$ if $A \leq 1$) and $2\tilde{R} < 2b_{01}/\tilde{s}_c$. We have demonstrated that such conditions may be realized in laboratory-scale systems or in low permeability formations. Moreover, our results have implications for numerical simulations of Cartesian geometries. They suggest that even if all fluid and rock properties are the same as in large domain, finer gridding may be necessary to capture the earliest-growing mode in domains where $\tilde{W}$ is small, especially if $A < 1$.
- When $A = 1$, patterns of the earliest-growing perturbation mode are symmetric about a reflection across $\tilde{y} = \tilde{x}$ and are three-dimensional in nature. In many cases, we see channels that are similar to those observed in the numerical study of Pau *et al.*[50] Two-dimensional modes tend to be preferred in geometries where the size in one horizontal dimension is small, while the size in the other horizontal dimension is much larger.
- In contrast, the patterns of the earliest-growing mode in cylindrical geometries are antisymmetric in the horizontal plane. The sinusoidal nature in θ creates alternating positive and negative regions of the perturbations that are distinct from the channeling seen in Cartesian geometries. For certain values of $2\tilde{R}$, the perturbations may be insignificant near the center of the cylinder at early times.
- Based on observations from earlier papers,[18,50,55] we hypothesize that the contrasts between the Cartesian and cylindrical patterns may lead to significantly different behavior (e.g., different CO_2 dissolution rates) in the two geometries after the onset time. In future studies, we may test this hypothesis by performing numerical simulations in cylindrical geometries. The simulations could be compared with the Cartesian geometry results from Pau *et al.*[50] and with our theoretical predictions. Our results suggest that a spectral or pseudospectral method may be ideal for solving the Poisson equation that governs the transient base state problem.

ACKNOWLEDGMENTS

Financial support for this work has been provided by the member companies of the Reservoir Engineering Research Institute.

[1] A. Pellew and R. V. Southwell, "On maintained convective motion in a fluid heated from below," Proc. R. Soc. London, Ser. A **176**, 312–343 (1940).
[2] B. R. Morton, "On the equilibrium of a stratified layer of fluid," Q. J. Mech. Appl. Math. **10**, 433–447 (1957).
[3] R. A. Wooding, "The stability of a viscous liquid in a vertical tube containing porous material," Proc. R. Soc. London, Ser. A **252**, 120–134 (1959).
[4] G. S. Charlson and R. Sani, "On thermoconvective instability in a bounded cylindrical fluid layer," Int. J. Heat Mass Transfer **14**, 2157–2160 (1971).
[5] C. Normand, Y. Pomeau, and M. G. Velarde, "Convective instability: A physicist's approach," Rev. Mod. Phys. **49**, 581–624 (1977).
[6] S. Rosenblat, "Thermal convection in a vertical circular cylinder," J. Fluid Mech. **122**, 395–410 (1982).
[7] R. Narayanan and A. E. Abasaeed, "The effects of domain size and fluid conditions at the boundary: On convection inside an annulus heated from below," Int. Commun. Heat Mass Transfer **12**, 287–298 (1985).
[8] F. Marqués, M. Net, J. Massaguer, and I. Mercader, "Thermal convection in vertical cylinders: A method based on potentials of velocity," Comput. Methods Appl. Mech. Eng. **110**, 157–169 (1993).
[9] C. R. Doering and P. Constantin, "Bounds for heat transport in a porous layers," J. Fluid Mech. **376**, 263–296 (1998).
[10] M. P. Dyko, K. Vafai, and A. K. Mojtabi, "A numerical and experimental investigation of stability of natural convective flows within a horizontal annulus," J. Fluid Mech. **381**, 27–61 (1999).
[11] M. P. Dyko and K. Vafai, "Three-dimensional natural convective states in a narrow-gap horizontal annulus," J. Fluid Mech. **445**, 1–36 (2001).

[12] M. P. Dyko and K. Vafai, "On the presence of odd transverse convective rolls in narrow-gap horizontal annuli," Phys. Fluids **14**, 1291–1294 (2002).
[13] C. W. Horton and F. T. Rogers, "Convection currents in a porous medium," J. Appl. Phys. **16**, 367–370 (1945).
[14] E. R. Lapwood, "Convection of a fluid in a porous medium," Math. Proc. Cambridge Philos. Soc. **44**, 508–521 (1948).
[15] S. Chandrasekhar, *Hydrodynamic and Hydromagnetic Stability* (Dover Publications, New York, 1981).
[16] D. A. Nield and A. Bejan, *Convection in Porous Media*, 3rd ed. (Springer, New York, 2006).
[17] J. L. Beck, "Convection in a box of porous material saturated with fluid," Phys. Fluids **15**, 1377–1383 (1972).
[18] A. Zebib and D. R. Kassoy, "Three-dimensional natural convection motion in a porous medium," Phys. Fluids **21**, 1–4 (1978).
[19] A. Zebib, "Onset of natural convection in a cylinder of water saturated porous media," Phys. Fluids **21**, 699–700 (1978).
[20] K. B. Haugen and P. A. Tyvand, "Onset of thermal convection in a vertical porous cylinder with conducting wall," Phys. Fluids **15**, 2661–2667 (2003).
[21] H. S. Nygård and P. A. Tyvand, "Onset of convection in a porous box with partly conducting and partly penetrative sidewalls," Transp. Porous Media **84**, 55–73 (2010).
[22] A. V. Kuznetsov and D. A. Nield, "The onset of double-diffusive convection in a vertical cylinder occupied by a heterogeneous porous medium with vertical throughflow," Transp. Porous Media **95**, 327–336 (2012).
[23] E. Lindeberg and D. Wessel-Berg, "Vertical convection in an aquifer column under a gas cap of CO_2," Energy Convers. Manage. **38**, S229 (1997).
[24] IPCC, "Special report on carbon dioxide capture and storage," Technical Report (World Meteorological Organization and the United Nations Environment Programme, 2005).
[25] A. Firoozabadi and P. Cheng, "Prospects for subsurface CO_2 sequestration," AIChE J. **56**, 1398–1405 (2010).
[26] J. Ennis-King and L. Paterson, "Role of convective mixing in the long-term storage of carbon dioxide in deep saline formations," SPE J. **10**, 349–356 (2005).
[27] M. C. Kim and S. Kim, "Convective instability in fluid-saturated porous layer under uniform volumetric heat sources," Int. Commun. Heat Mass Transfer **29**, 919–928 (2002).
[28] J. Ennis-King, I. Preston, and L. Paterson, "Onset of convection in anisotropic porous media subject to a rapid change in boundary conditions," Phys. Fluids **17**, 084107 (2005).
[29] X. Xu, S. Chen, and D. Zhang, "Convective stability analysis of the long-term storage of carbon dioxide in deep saline aquifers," Adv. Water Resour. **29**, 397–407 (2006).
[30] A. Riaz, M. Hesse, H. A. Tchelepi, and F. M. Orr, "Onset of convection in a gravitationally unstable diffusive boundary layer in porous media," J. Fluid Mech. **548**, 87–111 (2006).
[31] H. Hassanzadeh, M. Pooladi-Darvish, and D. W. Keith, "Stability of a fluid in a horizontal saturated porous layer: Effect of non-linear concentration profile, initial, and boundary conditions," Transp. Porous Media **65**, 193–211 (2006).
[32] A. Selim and D. A. S. Rees, "The stability of a developing thermal front in a porous medium. I Linear theory," J. Porous Media **10**, 1–16 (2007).
[33] S. Rapaka, S. Chen, R. J. Pawar, P. H. Stauffer, and D. Zhang, "Non-modal growth of perturbations in density-driven convection in porous media," J. Fluid Mech. **609**, 285–303 (2008).
[34] M. C. Kim, K. W. Song, C. K. Choi, and J.-K. Yeo, "Onset of buoyancy-driven convection in a liquid-saturated cylindrical porous layer supported by a gas layer," Phys. Fluids **20**, 054104 (2008).
[35] A. C. Slim and T. S. Ramakrishan, "Onset and cessation of time-dependent, dissolution-driven convection in porous media," Phys. Fluids **22**, 124103 (2010).
[36] P. Cheng, M. Bestehorn, and A. Firoozabadi, "Effect of permeability anisotropy on buoyancy-driven flow for CO_2 sequestration in saline aquifers," Water Resour. Res. **48**, W09539, doi:10.1029/2012WR011939 (2012).
[37] M. Bestehorn and A. Firoozabadi, "Effect of fluctuations on the onset of density-driven convection in porous media," Phys. Fluids **24**, 114102 (2012).
[38] G. M. Homsy, "Global stability of time-dependent flows: Impulsively heated or cooled fluid layers," J. Fluid Mech. **60**, 129–139 (1973).
[39] J. P. Caltagirone, "Stability of a saturated porous layer subject to a sudden rise in surface temperature: Comparison between the linear and energy methods," Q. J. Mech. Appl. Math. **33**, 47–58 (1980).
[40] W. Lick, "The instability of a fluid layer with time-dependent heating," J. Fluid Mech. **21**, 565–576 (1965).
[41] T. D. Foster, "Stability of a homogeneous fluid cooled uniformly from above," Phys. Fluids **8**, 1249–1257 (1965).
[42] T. D. Foster, "Effect of boundary conditions on the onset of convection," Phys. Fluids **11**, 1257–1262 (1968).
[43] T. D. Foster, "Onset of manifest convection in a layer of fluid with a time-dependent surface temperature," Phys. Fluids **12**, 2482–2487 (1969).
[44] P. Gresho and R. Sani, "The stability of a fluid layer subjected to a step change in temperature: Transient vs. frozen time analyses," Int. J. Heat Mass Transfer **14**, 207–221 (1971).
[45] Y. Ben, E. A. Demekhin, and H.-C. Chang, "A spectral theory for small-amplitude miscible fingering," Phys. Fluids **14**, 999–1010 (2002).
[46] D. A. S. Rees, A. Selim, and J. P. Ennis-King, "The instability of unsteady boundary layers in porous media," *Emerging Topics in Heat and Mass Transfer in Porous Media* (Springer, Dordrecht, 2008), Chap. 4, pp. 85–110.
[47] R. Farajzadeh, H. Salimi, P. Zitha, and H. Bruining, "Numerical simulation of density-driven natural convection in porous media with application for CO_2 injection projects," Int. J. Heat Mass Transfer **50**, 5054–5064 (2007).
[48] T. Kneafsey and K. Pruess, "Laboratory flow experiments for visualizing carbon dioxide-induced, density-driven brine convection," Transp. Porous Media **82**, 123–139 (2010).
[49] R. Nazari Moghaddam, B. Rostami, P. Pourafshary, and Y. Fallahzadeh, "Quantification of density-driven natural convection for dissolution mechanism in CO_2 sequestration," Transp. Porous Media **92**, 439–456 (2012).
[50] G. S. H. Pau, J. B. Bell, K. Pruess, A. S. Almgren, M. J. Lijewski, and K. Zhang, "High-resolution simulation and characterization of density-driven flow in CO_2 storage in saline aquifers," Adv. Water Resour. **33**, 443–455 (2010).

[51] J. J. Hidalgo and J. Carrera, "Effect of dispersion on the onset of convection during CO_2 sequestration," J. Fluid Mech. **640**, 441–452 (2009).
[52] M. Bestehorn, "Phase and amplitude instabilities for Bénard-Marangoni convection in fluid layers with large aspect ratio," Phys. Rev. E **48**, 3622–3634 (1993).
[53] D. Jackson, *Fourier Series and Orthogonal Polynomials* (Dover Publications, Mineola, 2004).
[54] W. W. Bell, *Special Functions for Scientists and Engineers* (Dover Publications, Mineola, 2004).
[55] P. H. Holst and K. Aziz, "Transient three-dimensional natural convection in confined porous media," Int. J. Heat Mass Transfer **15**, 73–90 (1972).